CHALMERS
UNIVERSITY OF TECHNOLOGY

Design and Control of Grid-tied Power Electronics Converter for Battery Energy Storage System

Master's thesis in Sustainable Electric Power Engineering and Electromobility

Chenzhi Fu

DEPARTMENT OF ELECTRICAL ENGINEERING
CHALMERS UNIVERSITY OF TECHNOLOGY
Gothenburg, Sweden 2025
www.chalmers.se

Master's thesis 2025

Design and Control of Grid-tied Power Electronics Converter for Battery Energy Storage System

CHENZHI FU

CHALMERS
UNIVERSITY OF TECHNOLOGY

Department of Electrical Engineering
Division of Electric Power Engineering
Chalmers University of Technology
Gothenburg, Sweden 2025

Design and Control of Grid-tied Power Electronics Converter for Battery Energy Storage System

CHENZHI FU

Supervisor: Anton Kersten, Volvo Penta
Examiner: Massimo Bongiorno, Department of Electrical Engineering

Master's Thesis 2025
Department of Electrical Engineering
Division of Electric Power Engineering
Chalmers University of Technology
SE-412 96 Gothenburg
Telephone +46 31 772 1000

Cover: A Battery Energy Storage System.

Typeset in LaTeX
Printed by Chalmers Reproservice
Gothenburg, Sweden 2025

Design and Control of Grid-tied Power Electronics Converter for Battery Energy Storage System

CHENZHI FU
Department of Electrical Engineering
Chalmers University of Technology

Abstract

Battery Energy Storage Systems (BESS) play a key role in supporting renewable energy integration and enabling grid services such as load balancing and backup power. This thesis compares two grid-tied power conversion systems for BESS applications: one using a traditional line-frequency transformer (LFT) for isolation, and another using a high-frequency transformer (HFT) integrated into Dual Active Bridge (DAB) converter.

Both systems are modeled and simulated in MTALAB and PLECS to evaluate their efficiency and suitability for high-power applications. The LFT system offers simplicity but suffers low efficiency at light load due to constant core losses. In contrast, the HFT-based system, using multiple parallel DAB converters, maintains consistently high efficiency across a wide power range and supports a more compact, scalable design.

The results highlight the trade-offs between LFT and HFT approaches in terms of power density, efficiency, and flexibility, providing guidance for future BESS designs in grid-connected environments.

Keywords: BESS, Power Electronics, DAB Converter, Inverter, Transformer, Galvanic Isolation, Grid Integration.

Acknowledgements

I would like to thank the ESS team at Volvo Penta for their support and for giving me the opportunity to work on this thesis. I am especially grateful to my supervisor Anton Kersten for his guidance, encouragement, and helpful feedback throughout the project. I also want to thank Professor Massimo Bongiorno, my academic supervisor at Chalmers, for his valuable input and support during the thesis. Your help has been truly appreciated.

Chenzhi Fu, Gothenburg, June 2025

List of Acronyms

Below is the list of acronyms that have been used throughout this thesis listed in alphabetical order:

AC	Alternating current
BESS	Battery Energy Storage System
DAB	Dual Active Bridge
DC	Direct current
EMC	Electromagnetic Compatibility
HFT	High Frequency Transformer
LFT	Line Frequency Transformer
NPC	Neutral Point Clamped
PI	Proportional integral
PLL	Phase-locked Loop
PR	Proportional Resonant
PWM	Pulse-width Modulation
THD	Total Harmonic Distortion
VSI	Voltage Source Inverter

Contents

List of Acronyms **ix**

List of Figures **xiii**

List of Tables **xv**

1 Introduction **1**
1.1 Background . . . 1
1.2 Objective . . . 2
1.3 Limitation . . . 2

2 Theory **3**
2.1 Grid-Tied Inverters system in BESS . . . 3
2.1.1 Challenges of Grid Integration . . . 3
2.1.2 Electrical Conversion Topologies . . . 3
2.1.3 Converter Control Techniques . . . 5
2.1.3.1 PR Control for the Grid-Tied Inverter . . . 5
2.1.3.2 Phase Shift Control for the DAB Converter . . . 6
2.1.4 LCL Filter Design . . . 7
2.1.5 Equivalent Circuit of Transformer . . . 8
2.2 Loss Models in Power Electronics . . . 10
2.2.1 Semiconductor Losses . . . 10
2.2.2 Transformer and Filter Losses . . . 11

3 Methods **13**
3.1 System Overview . . . 13
3.2 LFT-based System Design . . . 15
3.2.1 System Schematics . . . 15
3.2.2 PR Control Implementation . . . 18
3.2.3 Parameters of Transformer Equivalent Circuit . . . 19
3.2.4 LCL Filter Design . . . 20
3.3 HFT-based System Design . . . 21
3.3.1 DAB Converter Model . . . 21
3.3.1.1 DAB Converter Schematics . . . 21
3.3.1.2 DAB Converter Parameters . . . 23
3.3.1.3 Phase Shift Control . . . 25
3.3.2 Inverter Stage Schematics . . . 26

4 Results **29**
4.1 Overview of Simulation 29
4.2 Control Performance Evaluation 29
4.2.1 PR Controller Performance (Both Systems) 29
4.2.2 DAB Phase Shift Control (HFT System) 31
4.3 Efficiency 31
4.3.1 LFT System Efficiency 31
4.3.1.1 Results 31
4.3.1.2 Discussion 33
4.3.2 HFT System Efficiency 34
4.3.2.1 Results 34
4.3.2.2 Discussion 36
4.3.3 LFT vs. HFT(DAB) 36
4.3.3.1 Results 36
4.3.3.2 Discussion 38

5 Conclusion **39**

Bibliography **41**

List of Figures

2.1 Block diagram of DC fast charging with: (a) line-frequency transformer, (b) high-frequency transformer 4
2.2 Three-phase grid inverter current control using PR controller 6
2.3 Topology of DAB Converter 6
2.4 Single-phase LCL filter configuration with internal resistances of filter inductors 8
2.5 Transformer Equivalent Circuit referred to Primary Side 8

3.1 Topology of Line-frequency Transformer-based System 13
3.2 Topology of High-frequency Transformer-based System a. With 2-level inverter b. With 3-level NPC inverter 14
3.3 LFT-based System Schematics with Two types of Inverter (a) 2-level inverter, (b) 3-level NPC inverter 17
3.4 Current Control with PR Controller for single phase 18
3.5 Space Vector modulation for 2-level VSI 19
3.6 Equivalent Ciruit Design of 3-Phase Line-frequency Transformer . . . 20
3.7 Ciruit Design of 3-Phase LCL Filter 21
3.8 DAB Converter Schematic 22
3.9 Leakage Test Setups 24
3.10 Transformer Leakage Inductance vs. Frequency 24
3.11 Phase Shift Controller 25
3.12 HFT-based System Schematics with Two types of Inverter (a) 2-level inverter, (b) 3-level NPC inverter 28

4.1 3-phase Current Waveform (a). With 2-level inverter (b). With 3-level NPC inverter 30
4.2 Output Voltage of DAB Converter 31
4.3 Overall Efficiency of LFT System a. With 2-level inverter b. With 3-level NPC inverter 32
4.4 Efficiency of DAB Converter 34
4.5 Efficiency Curves a. With 2-level inverter b. With 3-level NPC inverter 35
4.6 Efficiency Curve of a. Line Frequency Transformer b. Parallel DAB Converter 37

List of Tables

2.1 Comparison of LFT and HFT Systems 4

3.1 Results of Transformer Tests 19
3.2 Parameters of Transformer Equivalent Circuit 19
3.3 Parameters of LCL Filter 20
3.4 Parameters of Hysteretic Core 25

4.1 General Setup of LFT and HFT System 29

1
Introduction

This chapter presents the background, objectives and limitation of the thesis. It introduces the role of Battery Energy Storage Systems (BESS) in modern power grid, emphasizing their importance in energy flexibility and grid support. The chapter also outlines the challenges in power conversion and isolation for grid integration, particularly focusing on transformer-based solutions. Finally, it defines the scope of the work, addressing the limitations.

1.1 Background

The increasing integration of renewable energy sources, such as solar and wind, into modern power grids presents significant challenges in terms of energy reliability and stability[1]. Unlike conventional fossil-fuel-based generation, renewable energy sources are inherently unstable, leading to fluctuation in power supply. BESS have emerged as a crucial technology to mitigate these challenges by providing energy storage and grid stabilization[2].

BESS enables energy to be stored during periods of excess generation and supplied during peak demand, improving the efficiency and resilience of power systems[3]. These systems are widely used in various applications, including grid support, peak shaving, and frequency regulation[4][5]. Furthermore, BESS plays a key role in charging stations for electric vehicles (EVs), allowing efficient energy management and reducing the impact of high power demand on the grid[6].

A critical component of BESS is power electronics, which ensures efficient energy conversion between the battery and the grid. In particular, grid-tied converters are essential for converting the direct current (DC) from batteries into an alternating current (AC) suitable for grid integration[7]. These converters must comply with grid standards while ensuring minimal harmonic distortion, and effective control strategies for stable operation.

To enhance safety and performance, modern BESS inverters often incorporate transformers, which provide galvanic isolation between the grid and the battery system. This isolation prevents direct electrical connections that could lead to ground faults or safety hazards, making transformers a key consideration in the design of efficient and reliable storage systems[8].

1.2 Objective

This thesis focuses on the design and control of grid-tied power electronic converters for BESS, with an emphasis on energy efficiency, power density, and loss modeling. By developing a simulation model that accounts for key factors such as semiconductor switching losses, transformer efficiency, and grid filter losses, this work aims to provide insights into the optimal design of next-generation battery storage converters.

1.3 Limitation

This thesis is limited to simulation-based analysis and does not include experimental validation of the proposed systems. The DAB converter is based on a actual hardware prototype and modeled as a single unit in detail, while the parallel operation of multiple DAB modules is simplified using sequential activation without dynamic control. Additionally, the high-frequency transformer is modeled using idealized magnetic domain representations, and thermal effects, electromagnetic interference (EMI), and hardware constraints are not considered. Reliability aspects of the power converter systems were not considered, so factors such as thermal stress, component aging, and fault tolerance were beyond the scope of this work. These simplifications allow for focused efficiency and performance comparisons but may not capture all practical challenges.

2

Theory

This chapter provides the theoretical foundation for the design and control of a grid-tied inverter system for BESS. It covers the essential concepts of battery storage integration, grid-tied inverter operation, and transformer-based isolation. The chapter also discusses the control strategies employed in the system ensuring efficient power transfer and grid compliance. Furthermore, a comprehensive loss model is introduced to evaluate the system's efficiency.

2.1 Grid-Tied Inverters system in BESS

BESS requires efficient power conversion interfaces to connect with the grid. Since batteries store energy in DC form, an inverter is necessary to convert it into AC for grid integration. A grid-tied inverters system serves this purpose by ensuring that the power drawn from or injected into the grid meets voltage and frequency requirements while maintaining stability and efficiency.

2.1.1 Challenges of Grid Integration

The inverters system synchronize with the grid to inject or absorb power as needed. Unlike off-grid inverters, grid-tied systems require precise phase-locked loop (PLL) synchronization and compliance with grid codes to maintain stability and minimize total harmonic distortion (THD)[9]. A key design challenge in grid-tied inverters system is optimizing energy efficiency while ensuring power quality and grid support functionalities[10][11]. Switching and conduction losses in semiconductors, transformer core and copper losses, and grid filter losses must be minimized to enhance overall system performance.

2.1.2 Electrical Conversion Topologies

As shown in Fig 2.1, two common topologies are line-frequency transformer (LFT)-based system and high-frequency transformer (HFT)-based system using a DC-DC converter[12][13].

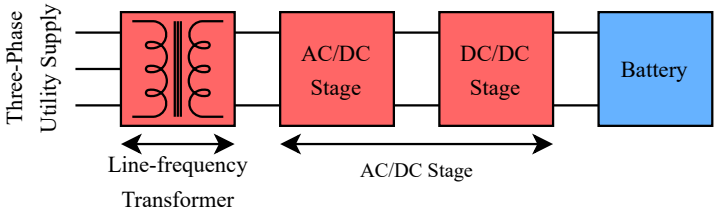

(a)

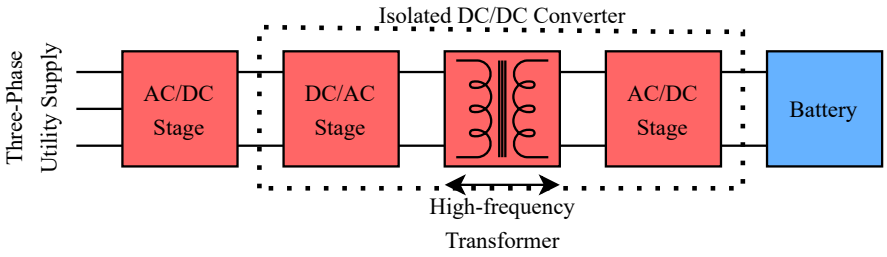

(b)

Figure 2.1: Block diagram of DC fast charging with: (a) line-frequency transformer, (b) high-frequency transformer

LFT-based system have a DC/DC stage, which is required to match the battery voltage and provide controlled charging and discharging, and also directly connect a voltage source inverter (VSI) to the grid, using a 50 Hz transformer for galvanic isolation. This approach ensures robustness and compliance with safety standards, but suffers from large size, heavy weight, and lower efficiency due to core losses[14]. In contrast, HFT-based inverters use a dual-active bridge (DAB) converter to provide isolation at high frequencies (tens to hundreds of kHz), significantly reducing transformer size and weight while improving power density. However, HFT solutions introduce additional switching losses and require more complex control strategies[14][15].

Table 2.1: Comparison of LFT and HFT Systems

Type	**LFT System**	**HFT System**
Transformer Size and Weight	Large and heavy	Compact and lightweight
Efficiency	Lower due to core losses	Higher with reduced losses
Power Density	Low	High
Control Complexity	Moderate	High (due to DAB phase shift control)
Application Suitability	Suitable for large-scale stationary applications	Ideal for space-constrained or mobile applications

This thesis aims to develop a simulation model to compare these topologies in terms of energy efficiency and power density. By analyzing semiconductor losses, transformer characteristics, and grid filter dynamics, this study will provide insight into optimizing grid-tied converter designs for modern BESS applications.

2.1.3 Converter Control Techniques

In this study, key control objectives include regulating DC/AC and DC/DC, maintaining grid voltage and frequency compliance, and minimizing harmonic distortion[16][17]. Two control strategies are implemented: proportional-resonant (PR) control for the grid-tied inverter and phase shift control for the DAB converter.

2.1.3.1 PR Control for the Grid-Tied Inverter

The performance of a grid-tied inverter in BESS depends significantly on its control strategy, which ensures efficient power conversion, grid synchronization, and stability.

Unlike conventional proportional-integral (PI) controllers, which struggle with the presence of steady-state error in the stationary frame and the need to decouple phase dependency in three phase systems, PR control effectively compensates for steady-state errors at the fundamental frequency[18][19]. The PR controller introduces a resonant term tuned to the grid frequency, significantly improving harmonic rejection and dynamic response[18].

The standard PR controller is expressed in the frequency domain, and the term $\frac{K_r s}{s^2+w_0^2}$ introduces a resonant peak at f_0 ensuring zero steady-state error for sinusoidal references at this frequency.

$$G_{PR} = K_p + \frac{K_r s}{s^2 + w_0^2} \tag{2.1}$$

Where:
K_p is the proportional gain, which determines the system's response speed and stability.
K_r is the resonant gain, which amplifies the controller's response at the fundamental frequency.
$w_0 = 2\pi f_0$ is the fundamental grid angular frequency.

For illustration, Fig. 2.2 shows the inner current control scheme of a three-phase inverter. This thesis will implement the PR control strategy in inverter simulations, evaluating its performance under different battery conditions and load scenarios.

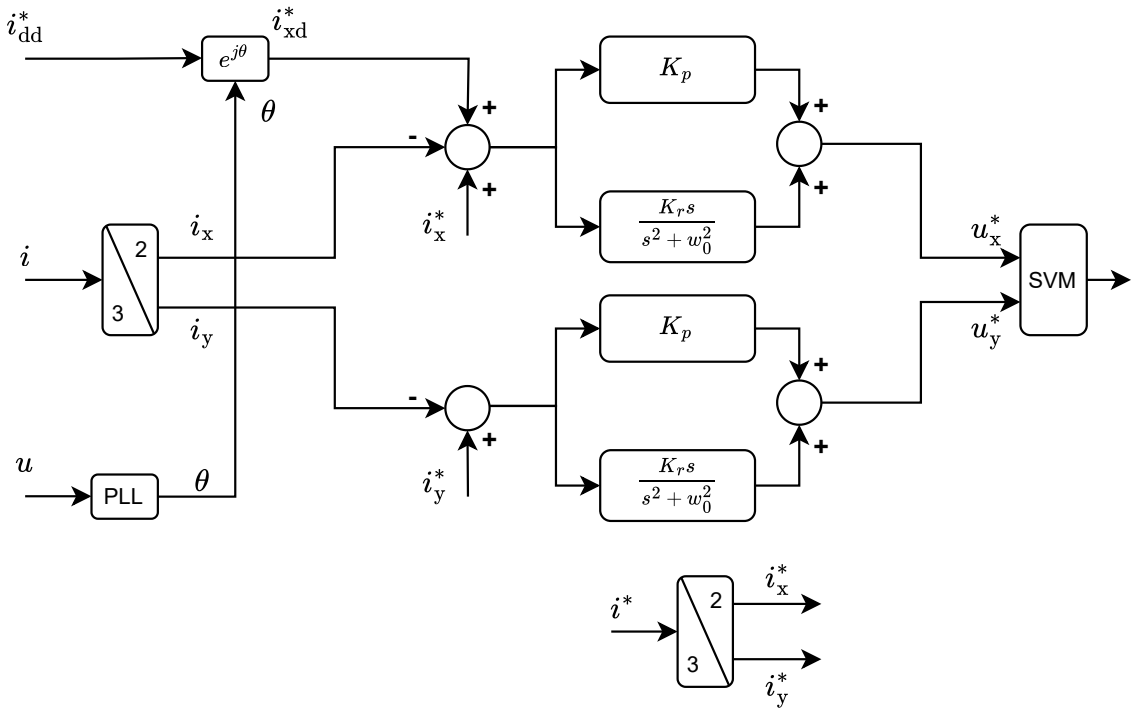

Figure 2.2: Three-phase grid inverter current control using PR controller

2.1.3.2 Phase Shift Control for the DAB Converter

The DAB converter is a widely used topology in high-frequency isolated power conversion systems, including BESS[20][21]. It consists of two full-bridge converters (one on the primary side and one on the secondary side) connected through a high-frequency transformer as shown in fig. 2.3. The power transfer is controlled by adjusting the phase shift between the AC voltage waveforms generated by the primary and secondary bridges.

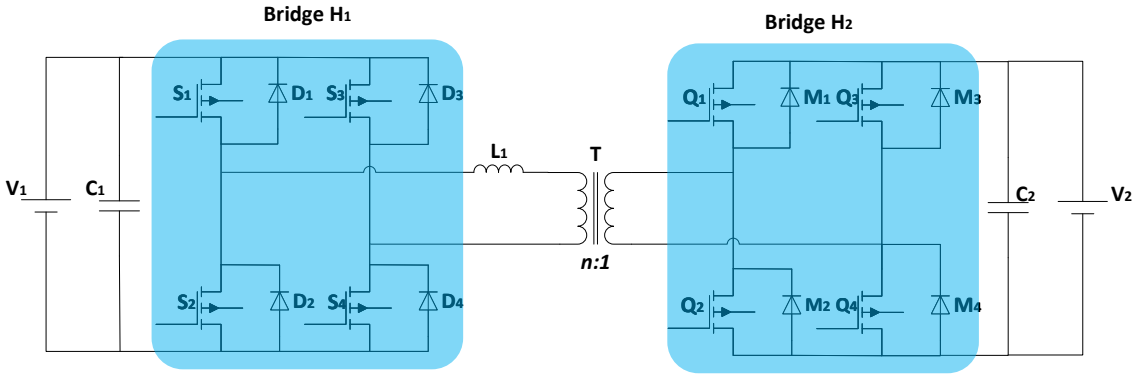

Figure 2.3: Topology of DAB Converter

The phase shift control of the DAB converter is implemented using a PI controller, which dynamically adjusts the phase shift angle (ϕ) to regulate the power flow, and the system computes the error signal:

$$e(t) = V^* - V_{\text{meas}} \tag{2.2}$$

Where:
V^* is the reference voltage level.
V_{meas} is the actual voltage measured by the sensor.

The continuous-time PI control law is:

$$\phi(t) = K_p e(t) + K_i \int e(t)dt \tag{2.3}$$

Where:
K_p is the proportional gain, controlling how aggressively ϕ reacts to changes.
K_i is the integral gain, ensuring zero steady-state error.

The computed phase shift (ϕ) is converted into a control signal using PWM modulation. A PWM generator modulates the gate signals of the full bridges, ensuring efficient operation[22]. In traditional PWM control, the cross-connected switch pairs in H-bridge (H_1), such as (S_1, S_4) and (S_2, S_3), are switched in turn to transform the high-voltage V_1 from DC to AC, the switches (Q_1–Q_4) in H-bridge (H_2) are turned OFF and the current conducts only through the diodes (M_1–M_4) to transform the voltage from AC to DC, so the power is transferred from V_1 side to V_2 side[23].

This thesis will simulate DAB converter using PI-controlled phase shift modulation, evaluating its impact on efficiency and ZVS operation under varying load conditions.

2.1.4 LCL Filter Design

Grid-tied inverters generate high-frequency switching waveforms that must be filtered before injecting power into the grid to ensure compliance with power quality standards. An LCL filter is commonly used to attenuate high-frequency harmonics and improve electromagnetic compatibility (EMC)[24][25].

Fig 2.4 shows a single-phase LCL filter configuration. It consists of:

- Inverter-side Inductor (L_{f}): Limits the switching ripple from the inverter.
- Grid-side Inductor (L_{g}): Ensures smooth current injection into the grid.
- Filter Capacitor (C_{f}): Forms a resonant circuit with the inductors to attenuate high-frequency harmonics.
- Damping Resistor (optional,R_{d}): Series connection on C_{f}, reduces resonance effects to improve stability.

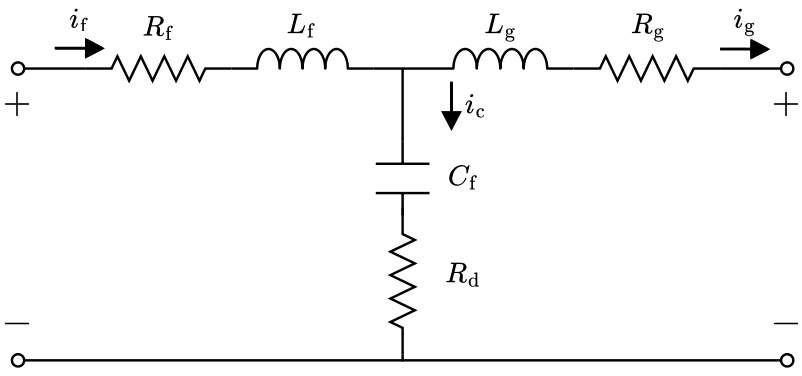

Figure 2.4: Single-phase LCL filter configuration with internal resistances of filter inductors

The LCL filter introduces a resonance peak at:

$$f_{\text{res}} = \frac{1}{2\pi}\sqrt{\frac{L_f + L_g}{L_f L_g C_f}} \tag{2.4}$$

This must be carefully designed to be below the switching frequency but above the fundamental grid frequency[26]. If a filter is not designed properly, it may not reduce noise as much as expected and could even make distortion worse due to unwanted oscillations.[27].

2.1.5 Equivalent Circuit of Transformer

In this study, the Line Frequency Transformer will be simulated as the form of T-equivalent circuit[28]. The T-equivalent circuit of a single-phase transformer is shown in Fig 2.5 .

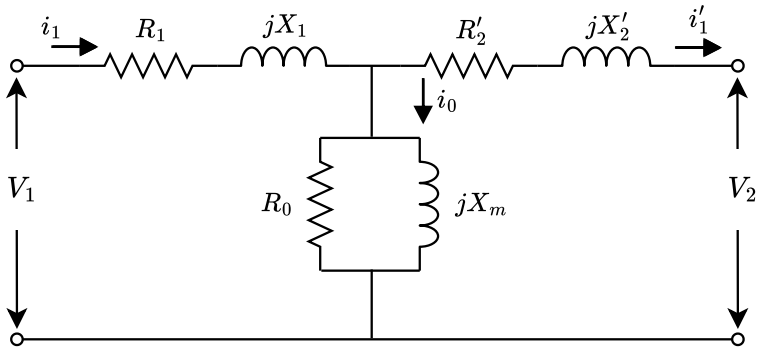

Figure 2.5: Transformer Equivalent Circuit referred to Primary Side

The parameters of equivalent circuit can be obtained by open-circuit and short-circuit measurement.

- Open-circuit Test
  In an open-circuit test, no current flows through the secondary winding (i'_1=0), meaning the secondary winding's leakage reactance (X'_2) and resistance (R'_2) do not influence the measurement. Additionally, the primary winding's resistance (R_1) and leakage reactance (X_1) are negligible compared to the magnetizing reactance (X_m) and magnetizing resistance (R_0), allowing them to be taken no account of.
  The open-circuit impedance can be calculated as follows:

$$Z_0 = \frac{R_0 \cdot X_\mathrm{m}}{R_0 + X_\mathrm{m}} = \frac{V_\mathrm{oc}}{I_\mathrm{oc}} \tag{2.5}$$

  Where:
  V_oc is the open-circuit voltage.
  I_oc is the open-circuit current.

  The open-circuit power factor $\cos\phi_0$ can be calculated from the open-circuit active power (P_oc):

$$\cos\phi_0 = \frac{P_\mathrm{oc}}{V_\mathrm{oc} I_\mathrm{oc}} \tag{2.6}$$

  The magnetizing resistance (R_0) and magnetizing reactance (X_m) can then be obtained using the following equations:

$$R_0 = \frac{Z_0}{\cos\phi_0} \tag{2.7}$$

$$X_\mathrm{m} = \frac{Z_0}{\sin\phi_0} \tag{2.8}$$

- Short-circuit Test
  In an short-circuit test, the load (V_2) is short-circuited. Since the winding resistances (R_1, R'_2) and leakage reactances (X_1, X'_2) are much smaller than the magnetizing reactance (X_m) and magnetizing resistance (R_0), the current through the magnetizing branch is negligible ($i_0 = 0$). So input current is almost equal to output current ($i_1 = i'_1$).
  The short-circuit impedance can be calculated as follows:

$$Z_0 = (R_1 + jX_1) + (R'_2 + jX'_2) = \frac{V_\mathrm{sc}}{I_\mathrm{sc}} \tag{2.9}$$

  Where:
  V_sc is the short-circuit voltage.
  I_sc is the short-circuit current.

  Similarly, The short-circuit power factor $\cos\phi_\mathrm{sc}$ can be calculated from the short-circuit power (P_sc):

$$\cos\phi_\mathrm{sc} = \frac{P_\mathrm{sc}}{V_\mathrm{sc} I_\mathrm{sc}} \tag{2.10}$$

The short-circuit resistance (R_{sc}) and short-circuit reactance (X_{sc}) can then be obtained using the following equations:

$$R_{\mathrm{sc}} = \frac{Z_{\mathrm{sc}}}{\cos \phi_{\mathrm{sc}}} \tag{2.11}$$

$$X_{\mathrm{sc}} = \frac{Z_{\mathrm{sc}}}{\sin \phi_{\mathrm{sc}}} \tag{2.12}$$

If the individual DC resistances are not specified, the leakage inductance and AC resistance can be assumed to be equally divided between the two windings[29]. The following equations apply:

$$R_1 = R_2' = R_2 \cdot n^2 = \frac{R_{\mathrm{sc}}}{2} \tag{2.13}$$

$$X_1 = X_2' = X_2 \cdot n^2 = \frac{X_{\mathrm{sc}}}{2} \tag{2.14}$$

Where:
n is the transformer ratio.

Magnetizing inductance (L_{m}), and leakage inductance (L_1, L_2') are calculated by the basic principal as follows:

$$L = \frac{X}{2\pi f} \tag{2.15}$$

Where:
f is the frequency of harmonic voltage.

2.2 Loss Models in Power Electronics

The efficiency of a grid-tied inverter system is influenced by various power losses, which mainly occur in semiconductors, transformers, and filters[30][31]. Accurately modeling these losses is essential for optimizing the energy efficiency and power density of the system. A comprehensive loss model considers semiconductor switching and conduction losses, transformer losses, and filter losses.

2.2.1 Semiconductor Losses

The power semiconductors (MOSFETs, IGBTs and antiparallel diode) in the inverter and the DAB converter contribute significantly to overall losses[31]. The power losses in the semiconductors in relation to the device current can be quantified as described in the following:

- Conduction Losses(P_{cond})
  It caused by the on-state resistance of MOSFETs or the voltage drop plus a resistive component in IGBTs, and can be estimated as:

$$P_{\text{cond,MOSFET}}(t) = R_{\text{DS(on)}} I^2(t) \qquad \text{(For MOSFETs)} \tag{2.16}$$

$$P_{\text{cond,IGBT}}(t) = R_{\text{CE}} I^2(t) + V_{CE(0)} I(t) \qquad \text{(For IGBTs)} \tag{2.17}$$

  Where:
  $I(t)$ is the instantaneous current through the switch.
  $R_{\text{DS(on)}}$ is MOSFET on-state resistance.
  R_{CE} is IGBT on-state resistance.
  $V_{\text{CE(0)}}$ is collector-to-emitter saturation voltage of IGBTs.
- Switching Losses(P_{sw})
  It occur during turn-on and turn-off due to voltage-current overlap, and can be approximately expressed as:

$$P_{\text{sw}}(t) = \frac{1}{2} V_{\text{dc}} I(t) (t_{\text{r}}(I(t)) + t_{\text{f}}(I(t))) f_{\text{sw}} \tag{2.18}$$

  Where:
  V_{dc} is the DC-link voltage.
  t_{r} t_{f} are the rise and fall times.
  f_{sw} is the switching frequency.

2.2.2 Transformer and Filter Losses

As long as a transformer is connected to the source, core losses are continuously generated in the magnetic core, regardless of the load. These losses result in heat buildup and are caused by hysteresis and eddy currents in the core material. In addition to core losses, copper losses caused by current flowing through the windings also contribute significantly to the overall transformer losses. They can be described as:

- Core Losses(P_{core})
  It can be estimated using the Steinmetz equation:

$$P_{\text{core}} = k f_{\text{sw}}^a B_{\text{pk}}^b V_{\text{core}} \tag{2.19}$$

  Where:

  f_{sw} is the frequency.
  B_{pk} is the peak magnetic flux density.
  V_{core} is the core's volume.
  k, a and b are material-dependent coefficients generally found from B-H hysteresis curve.
- Copper Losses(P_{cu})

$$P_{\text{cu}} = I_{\text{rms}}^2 R_{\text{winding}} \tag{2.20}$$

Where:
R_{winding} is the winding resistance.

The LCL filter introduces additional losses from:

- Inductor core and copper losses: Similar to transformer losses.
- Resistive damping losses: If a damping resistor is used, additional power dissipation occurs.

3
Methods

This chapter describes the systematic approach used to design, simulate, and evaluate the grid-tied inverter system with line-frequency transformer and high-frequency transformer isolated DAB converter. The methodology covers the development of the simulation model, control method implementation, and loss analysis.

3.1 System Overview

This thesis investigates two distinct BESS architectures for grid integration, differentiated by their transformer type and inverter topology. The first system uses a line-frequency transformer with a conventional inverter, while the second employs a high-frequency transformer integrated with a DAB converter. Additionally, two inverter topologies are evaluated for grid connection: a two-level voltage source inverter (VSI) and a three-level neutral-point clamped (NPC) inverter.

In the first architecture as Fig 3.1, a line-frequency transformer operates at 50 Hz to provide galvanic isolation between the battery and the grid. This system is directly connected to a two-level VSI or a three-level NPC inverter, which converts the DC battery voltage to AC for grid injection.

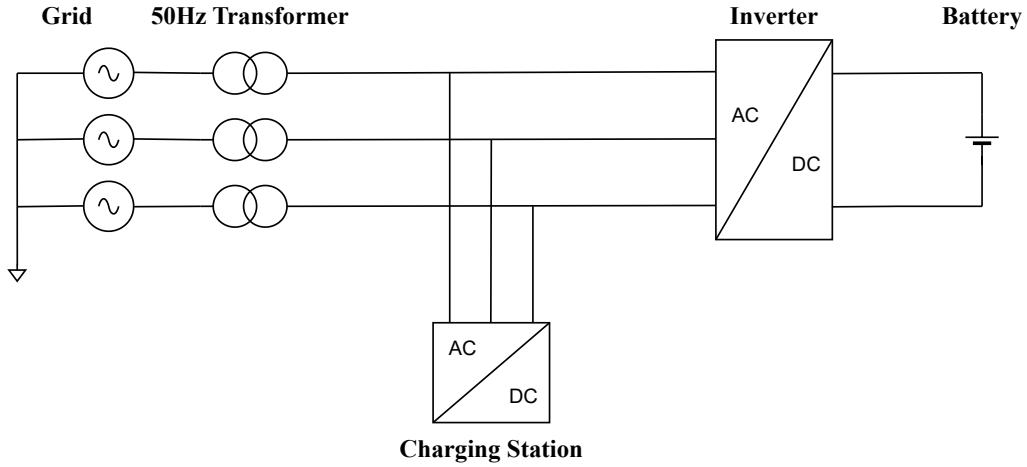

Figure 3.1: Topology of Line-frequency Transformer-based System

The second architecture shown in Fig 3.2 integrates a high-frequency transformer

within a DAB converter for DC-DC conversion and galvanic isolation. The HFT operates at tens to hundreds of kHz, significantly reducing the transformer's size and improving power density. The DAB converter uses phase shift control to regulate power flow between the battery and the inverter. After voltage conversion, the system employs a two-level VSI or a three-level NPC inverter for AC conversion and grid connection.

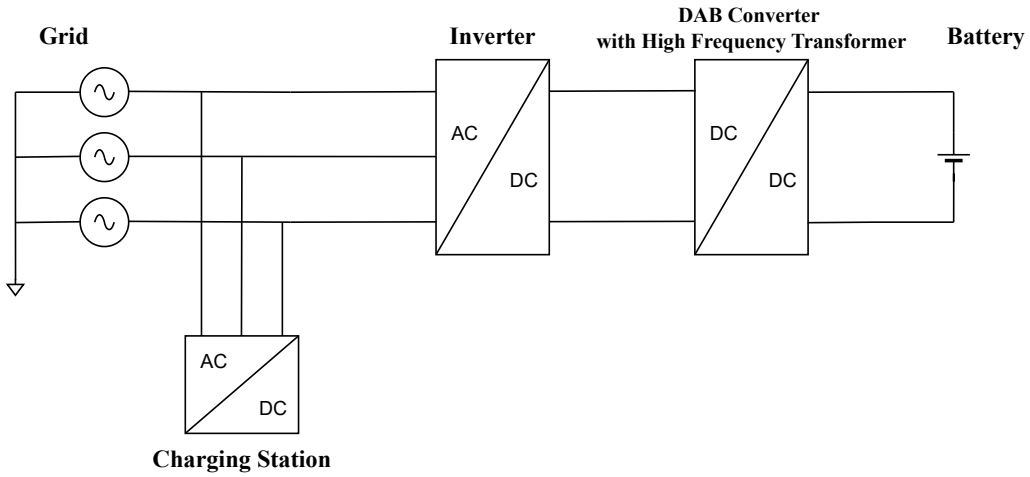

(a)

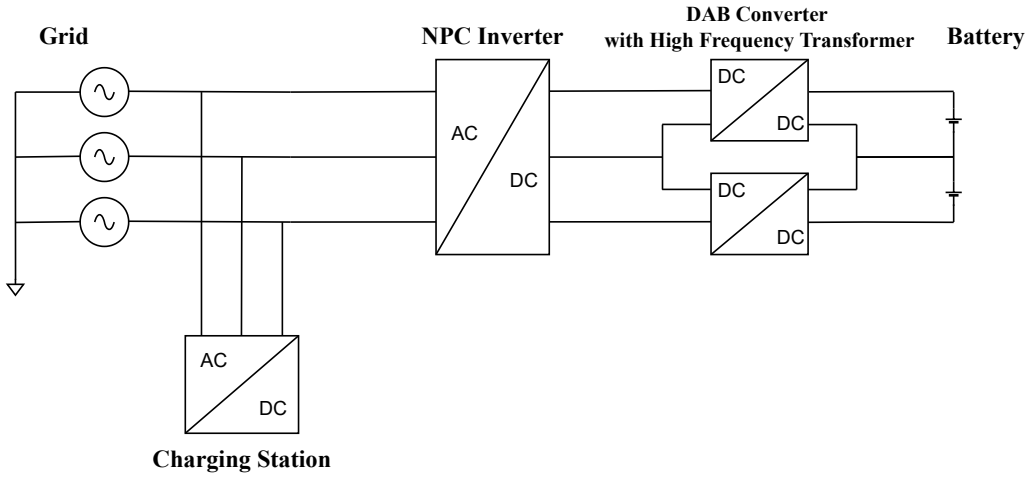

(b)

Figure 3.2: Topology of High-frequency Transformer-based System
a. With 2-level inverter
b. With 3-level NPC inverter

3.2 LFT-based System Design

3.2.1 System Schematics

The schematics of two LFT-based systems at PLECS are shown in Figure 3.3, and the model comprises the following subsystems:

1. DC Source (Battery)
   A controlled voltage source represents the battery pack with a variable output from 600 V to 750 V.
2. Inverter Stage
   Two inverter topologies were implemented for comparison:

   - 2-Level VSI
     A standard three-phase bridge with six SiC MOSFETs (Wolfspeed ECB4R-3M12YM3).
   - 3-Level NPC Inverter
     An enhanced topology with IGBT and clamping diodes (Vincotech 30-FT07NIA450S501-PD68F58), splitting the DC bus to reduce voltage stress on each switch.

3. LCL Filter
   The inverter output is connected to the grid via an LCL filter designed for 8 kHz switching frequency and <2% THD.
4. Line Frequency Transformer
   The transformer is modeled using a simplified equivalent circuit based on measured open-circuit and short-circuit test results.
5. Three-phase Grid Interface
   The grid is modeled as a balanced three-phase voltage source with fixed 400 V RMS at 50 Hz.

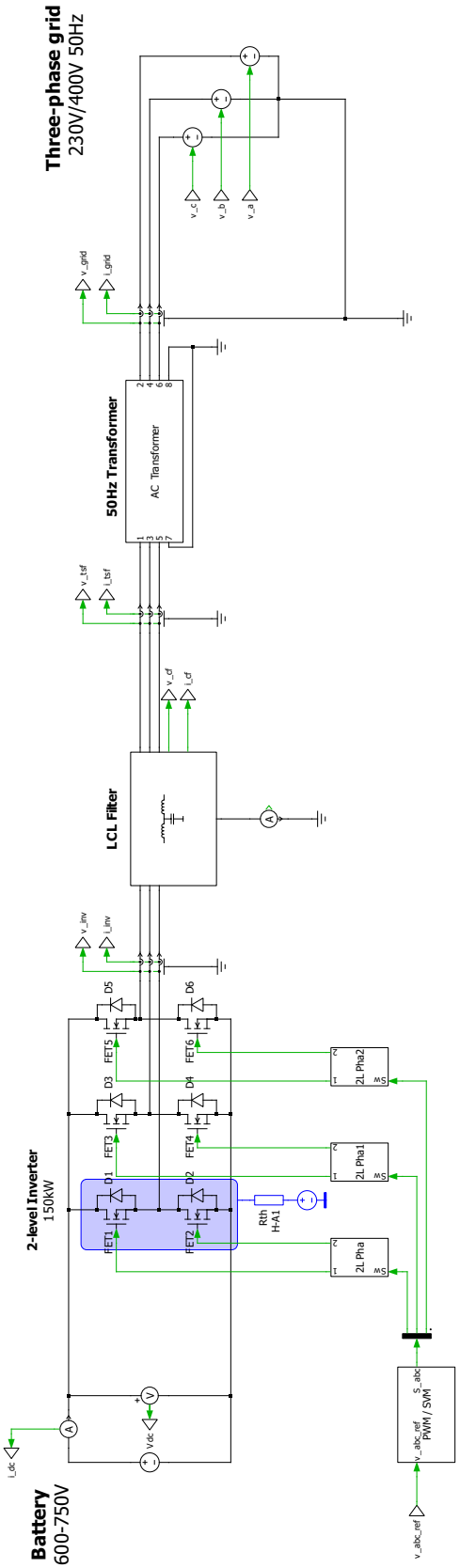
Three-phase grid
230V/400V 50Hz
v_c
v_b
v_a
v_grid
i_grid
50Hz Transformer
AC Transformer
v_tsf
i_tsf
v_cf
i_cf
LCL Filter
v_inv
i_inv
D5
D6
FET5
FET6
D3
D4
FET3
FET4
D1
D2
FET1
FET2
2-level Inverter
150kW
Rth
H-A1
2L Pha2
2L Pha1
2L Pha
S_abc
v_abc_ref
PWM / SVM
v_abc_ref
v_dc
i_dc
Battery
600-750V

(a)

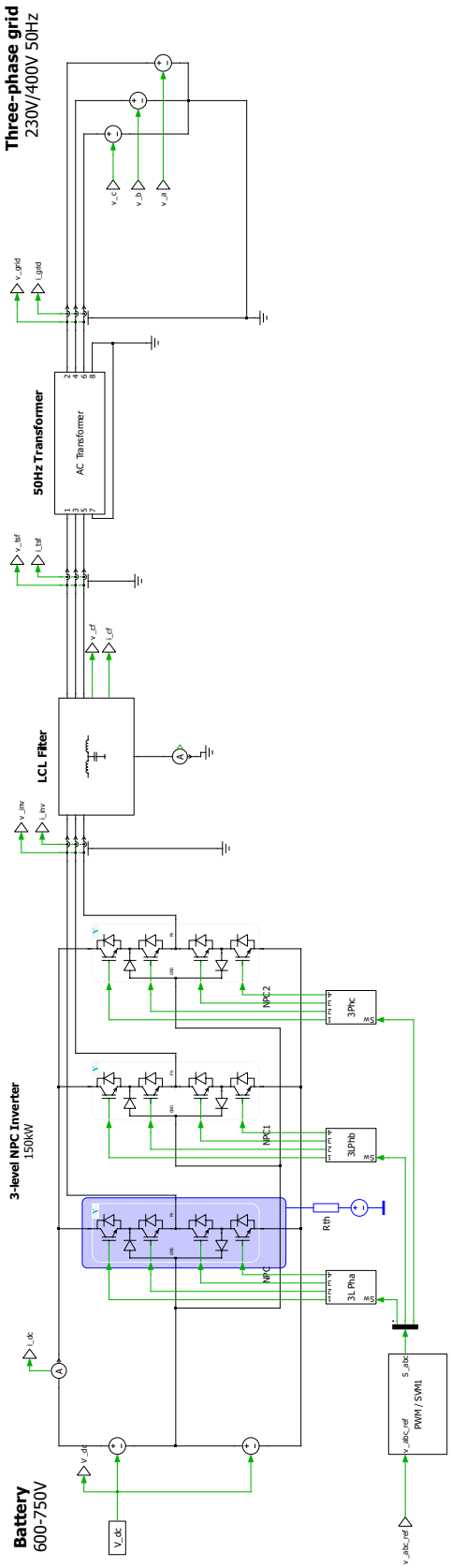

(b)

Figure 3.3: LFT-based System Schematics with Two types of Inverter (a) 2-level inverter, (b) 3-level NPC inverter

3.2.2 PR Control Implementation

The PR controller is used to regulate the inverter output current i_x to track a sinusoidal reference i_x^* with zero steady-state error at 50 Hz.

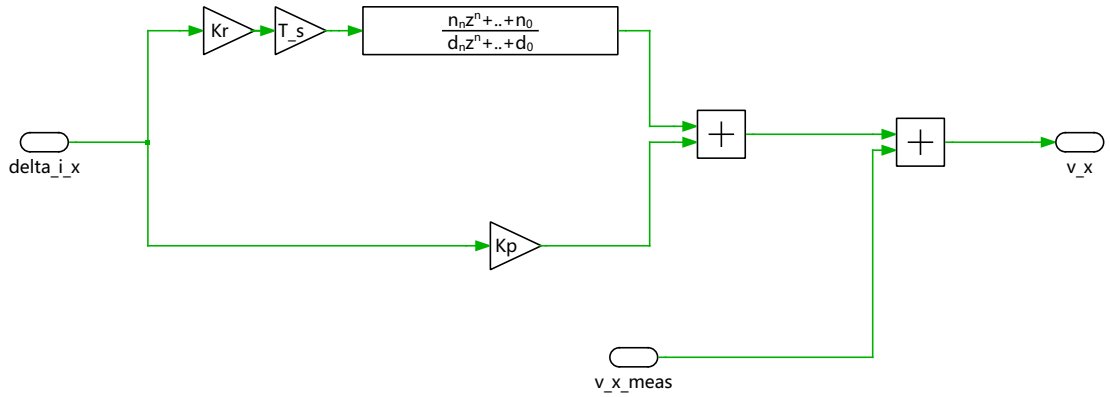

Figure 3.4: Current Control with PR Controller for single phase

The center frequency of resonance ω_0 is set to match the grid frequency 50 Hz, so the PR controller gives very high gain to eliminate steady-state error. The PR controller gains are tuned using the parameters of the LCL filter, specifically the inverter-side inductance L_f, grid-side inductance L_g, and inverter-side resistance R_f. The tuning procedure is as follows:

1. Controller Gain in Z-domain: The resulting gain $G_c(s)$ transformed into z-domain[32]
$$G_c(z) = K_p + K_r T_s \frac{z-1}{z^2 - z(2-\omega_0^2 T_s^2) + 1} \tag{3.1}$$
2. Crossover Frequency Selection: The desired crossover frequency α_c is chosen as one-tenth of the switching frequency.
$$\alpha_c = \frac{f_{sw}}{10} \tag{3.2}$$
Where: $f_{sw} = 8000$ Hz
3. Proportional Gain:
$$K_p = 1.5 \cdot (L_f + L_g) \cdot \alpha_c \tag{3.3}$$
4. Resonant Gain:
$$K_r = 1.5 \cdot R_f \cdot \alpha_c \tag{3.4}$$

This method ensures that the closed-loop bandwidth remains below the LCL filter's resonance frequency.

The PR controller is paired with Space Vector Pulse Width Modulation (SVPWM) to generate switching signals for both types of inverters.

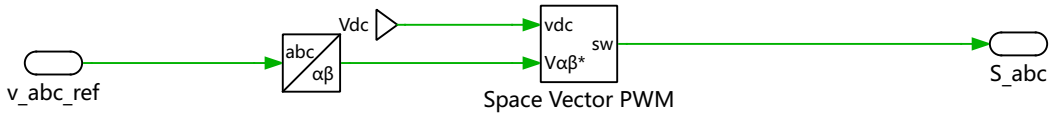

Figure 3.5: Space Vector modulation for 2-level VSI

3.2.3 Parameters of Transformer Equivalent Circuit

To model the line-frequency transformer (35394, C.T.S. trasformatori) in the LFT-based system, its equivalent circuit parameters are determined through standard open-circuit and short-circuit tests. The test results can be seen as below:

Table 3.1: Results of Transformer Tests

Type	**Input/Output Voltage (V)**	**Current (A)**	**Losses (W)**
Open Circuit Test	400/418	4.5	530
Short Circuit Test	-/-	216	3.95

The circuit parameters for single-phase can be calculated as:

Table 3.2: Parameters of Transformer Equivalent Circuit

Turns ratio	1:1
Primary winding resistance R_1 (Ω)	4.23×10^{-5}
Primary winding leakage inductance L_1 (H)	1.1×10^{-3}
Secondary winding resistance R_2 (Ω)	4.23×10^{-5}
Secondary winding leakage inductance L_2 (H)	1.1×10^{-3}
Magnetizing resistance R_0 (Ω)	301.89
Magnetizing inductance L_{m} (H)	2.96×10^{-3}

The calculated parameters are used in the transformer model in PLECS, enabling the simulation to capture losses, leakage behavior, and performance effects.

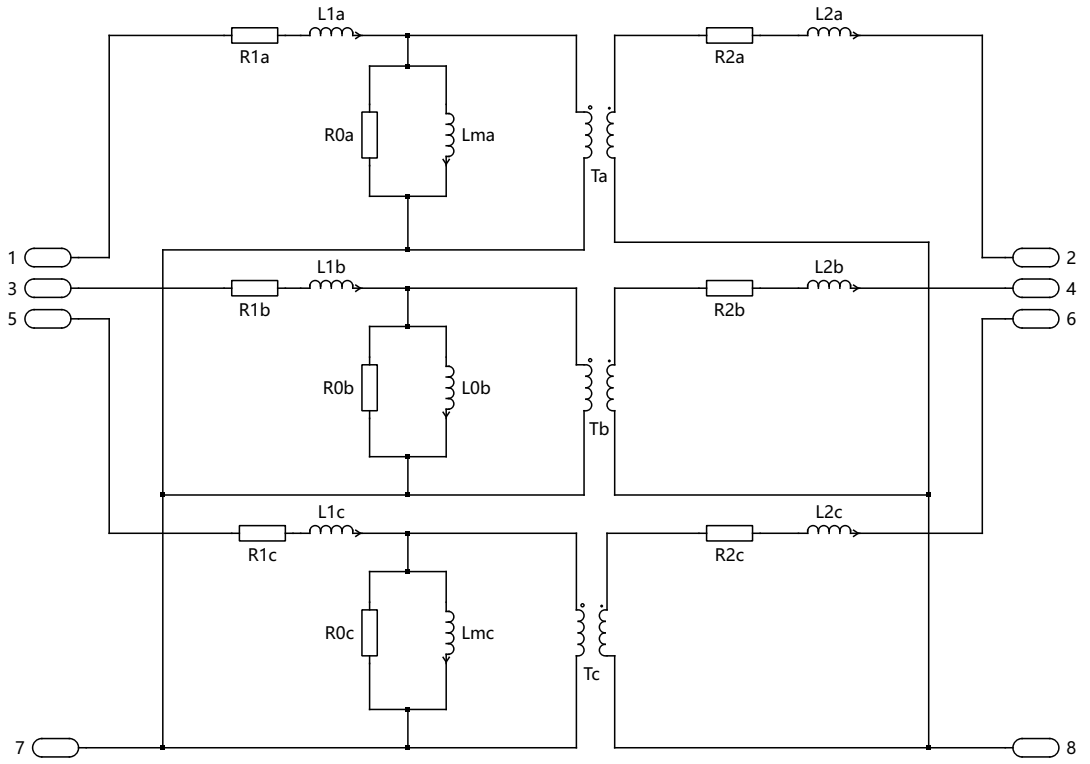

Figure 3.6: Equivalent Ciruit Design of 3-Phase Line-frequency Transformer

3.2.4 LCL Filter Design

The parameters used in the LCL filter design were guided by the specifications of a commercially available grid filter series, the Mangoldt PSF product line, and the capacitor value were increased for better performance.

Table 3.3: Parameters of LCL Filter

Inverter-side Inductor L_{f} (H)	0.14×10^{-3}
Inverter-side Resistor R_{f} (Ω)	4.1×10^{-3}
Grid-side Inductor L_{g} (H)	0.06×10^{-3}
Grid-side Resistor R_{g} (Ω)	4.1×10^{-3}
Filter Capacitor C_{f} (F)	180×10^{-6}

The resonant frequency of the filter is calculated as:

$$f_{\mathrm{res}} = \frac{1}{2\pi}\sqrt{\frac{L_{\mathrm{f}} + L_{\mathrm{g}}}{L_{\mathrm{f}} L_{\mathrm{g}} C_{\mathrm{f}}}} = \frac{1}{2\pi}\sqrt{\frac{0.00014 + 0.00006}{0.00014 \cdot 0.00006 \cdot 0.00018}} \approx 1.8 \quad \text{kHz} \tag{3.5}$$

So the designed LCL filter has a calculated resonant frequency of 1.8 kHz, which satisfies the requirement of being below the inverter's switching frequency (8 kHz) while remaining well above the fundamental grid frequency (50 Hz). This placement ensures that the filter effectively attenuates switching harmonics without interfering with the control bandwidth or introducing low-frequency resonance near the grid

frequency. The schematics of full three-phase filter is shown in Figure 3.7, where each phase is symmetrically designed.

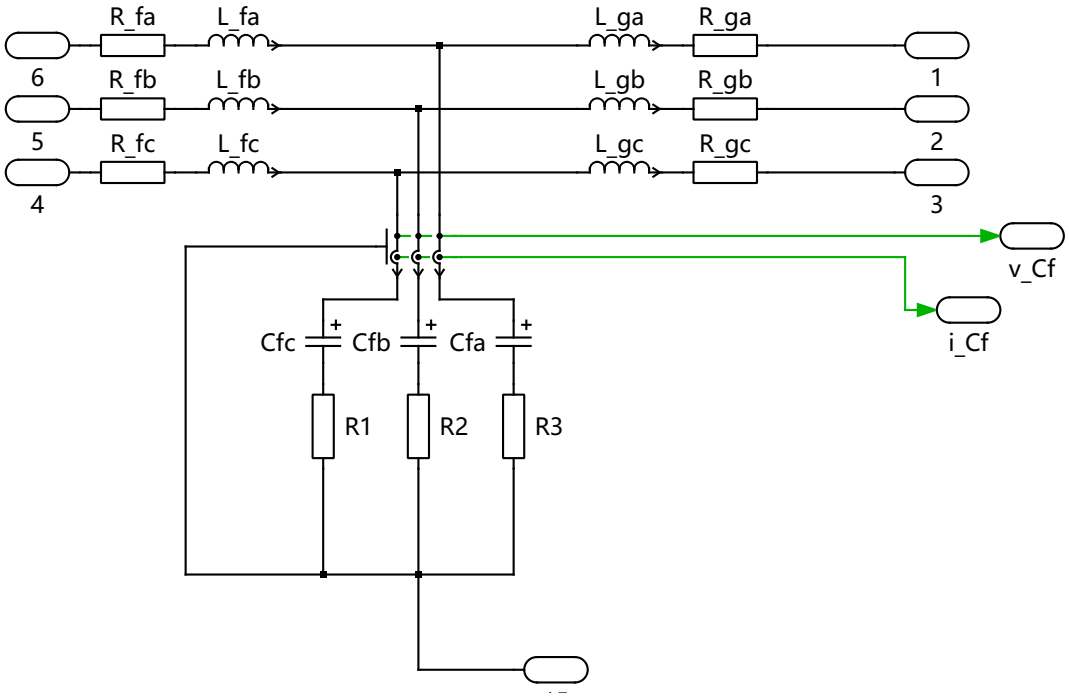

Figure 3.7: Ciruit Design of 3-Phase LCL Filter

3.3 HFT-based System Design

In this system, the battery pack is directly connected to the DAB converter on the input DC side. The DAB performs bidirectional power conversion and galvanic isolation through a high-frequency transformer. The DC output of the DAB feeds into a grid-tied inverter, which injects AC power into the grid via an LCL filter.

This system contains multiple DAB converters in parallel, which involves complex control techniques that are not discussed in this thesis. When it comes to efficiency analysis, the DAB will be assumed to be activated in sequence. Therefore, the DAB converter and inverter systems will be analyzed separately.

3.3.1 DAB Converter Model

3.3.1.1 DAB Converter Schematics

The DAB converter is simulated in PLECS and the schematic in figure 3.8 consists of:

- Two full-bridge inverters (primary and secondary sides)
- An interconnecting series inductance
- A high-frequency transformer simulated in the magnetic domain

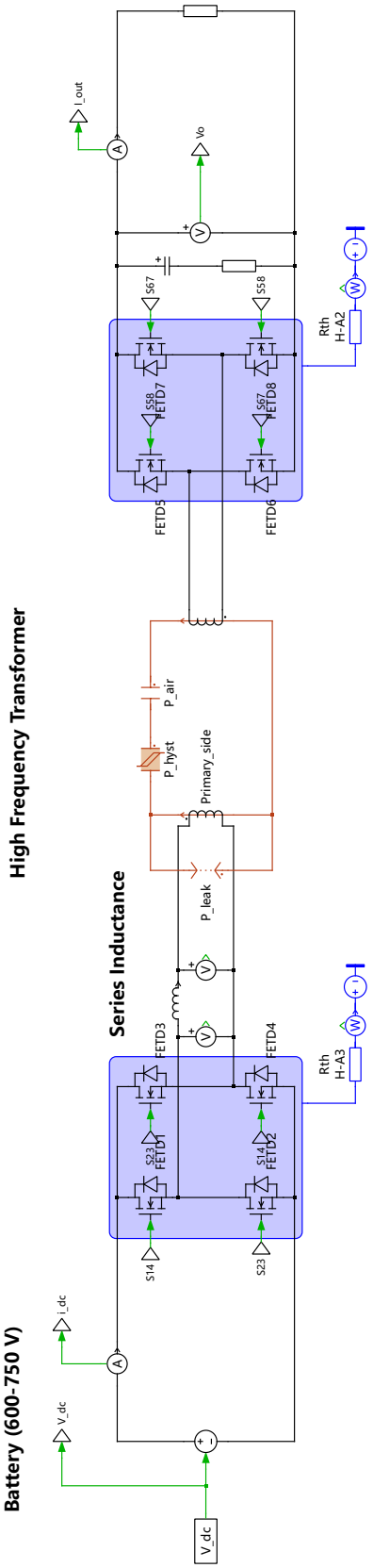

Figure 3.8: DAB Converter Schematic

3.3.1.2 DAB Converter Parameters

For the active switches in the DAB converter, the Infineon F4-11MR12W2M1H-B70 SiC MOSFET module was selected. This device is well-suited for BESS applications due to its 1200 V voltage rating, low switching losses, and good thermal performance.

The series inductance (including transformer leakage and any added discrete inductance) is crucial for controlling power flow. It is determined based on the desired maximum power transfer, the DC voltage levels, and the switching frequency. Using the DAB power equation for peak power transfer at a phase shift $\phi = \pi/2$:

$$P_{\max} = \frac{nV_1V_2}{8f_{\text{sw}}L_{\max}} \tag{3.6}$$

Where:
$n = 1$
$P_{\max} = 30\text{kW}$
$V_1 = 600$ V, $V_2 = 750$ V
$f_{\text{sw}} = 98000$ Hz

Solving for L:

$$L_{\max} = \frac{V_1V_2}{8f_{\text{sw}}P_{\max}} = \frac{600 \cdot 750}{8 \cdot 98000 \cdot 30000} \approx 19.1\mu H \tag{3.7}$$

Therefore, the total interconnection inductance must be carefully limited below this value, as exceeding the threshold will prevent the DAB converter from transferring its rated power of 30 kW reliably. If the inductance is too high, it reduces the power transfer capability and may lead to instability.

To confirm this, the actual transformer in DAB module was tested using the Analog Discovery 2 device. By applying a low-amplitude AC test signal to one winding while shorting the secondary, the leakage inductance was measured using impedance frequency sweep. The test environment is shown in Figure 3.9.

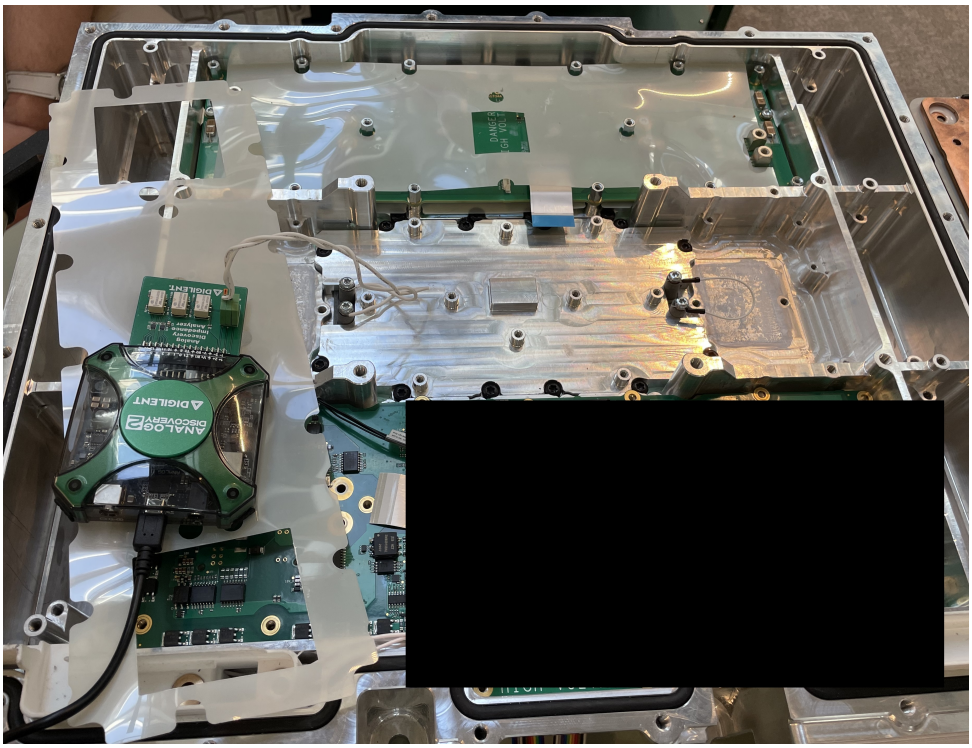

Figure 3.9: Leakage Test Setups

Figure 3.10 illustrates the measured inductance of the transformer winding as a function of frequency. The flat region around the possible operating frequency (50–100 kHz) suggests that the core and winding behave linearly and predictably within the DAB's switching frequency range, validating the selection of the transformer design for high-frequency operation.

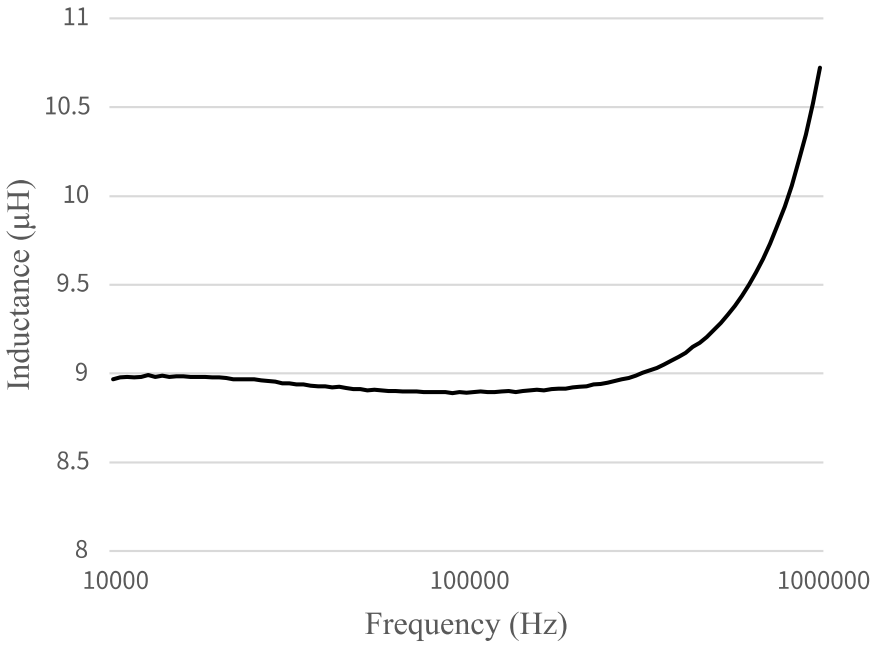

Figure 3.10: Transformer Leakage Inductance vs. Frequency

The measured value at designed frequency 98 kHz was:

$$L_{\text{leak,measured}} = 8.89\mu H \tag{3.8}$$

This value matches the theoretical requirement, confirming the suitability of the physical transformer for the DAB converter.

The transformer is modeled in the magnetic domain to accurately reflect nonlinear magnetic behavior. A ferrite core is selected based on standard industry components. The parameters of the core are below:

Table 3.4: Parameters of Hysteretic Core

Cross-sectional Area (m^2)	1000×10^{-6}
Length of Flux Path (m)	260×10^{-3}
Coercitive Field Strength H_{c} (A/m)	13
Remanence Flux Density B_{r} (T)	150×10^{-3}
Saturation Field Strength H_{sat} (A/m)	250
Saturation Flux Density B_{sat} (T)	500×10^{-3}
Saturation Rel. permeability $\mu_{\text{r,sat}}$	1000

3.3.1.3 Phase Shift Control

The primary control objective is to maintain a regulated DC-link voltage (750 V) at the output of the DAB under varying load conditions. The controller adjusts the phase shift angle ϕ based on the deviation between the measured output voltage V_{o} and a fixed reference $V_{\text{o,ref}}$.

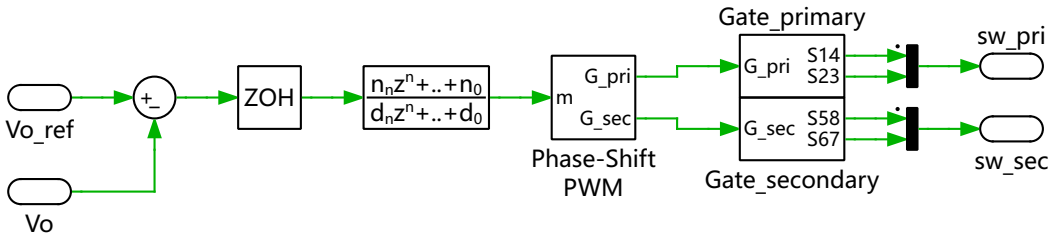

Figure 3.11: Phase Shift Controller

The phase shift controller is built using a standard proportional-integral (PI) structure, and the transfer function can be expressed as:

$$PI(s) = K_{\text{p}} + \frac{K_{\text{i}}}{s} \tag{3.9}$$

K_{p}, K_{i} are controller gains. A conservative tuning, which provides a good trade-off between fast transient response and smooth switching behavior, is chosen to ensure stability:

$K_\mathrm{p} = 0.11173 \cdot 0.015$
$K_\mathrm{i} = 0.11173$

Modern power converter control systems are implemented using digital signal processors (DSP), so it must be converted to a discrete-time representation in order to be implemented in DSP controllers [33]. It can be rewritten in the z-domain.

$$PI(z) = \frac{b_0 + b_1 z^{-1} + b_2 z^{-2}}{a_0 + a_1 z^{-1} + a_2 z^{-2}} \tag{3.10a}$$

$$b_0 = K_\mathrm{p}(1 + NT_\mathrm{s}) + K_\mathrm{i}T_\mathrm{s}(1 + NT_\mathrm{s}) \tag{3.10b}$$

$$b_1 = -(K_\mathrm{p}(2 + NT_\mathrm{s}) + K_\mathrm{i}T_\mathrm{s}) \tag{3.10c}$$

$$b_2 = K_\mathrm{p} \tag{3.10d}$$

$$a_0 = 1 + NT_\mathrm{s} \tag{3.10e}$$

$$a_1 = -(2 + NT_\mathrm{s}) \tag{3.10f}$$

$$a_2 = 1 \tag{3.10g}$$

Where: $N = 0$

3.3.2 Inverter Stage Schematics

The inverter subsystem in the HFT-based configuration is similar to the LFT-based system but with two key differences:

- The input voltage is fixed at 750 V DC, supplied by the DAB output.
- There is no line-frequency transformer between the inverter and the grid.

The main components of the system include:

- Voltage Source
  It represents fixed 750 V voltage output regulated by DAB converters.
- Inverter Stage
- LCL Filter
- Three-phase Grid Interface

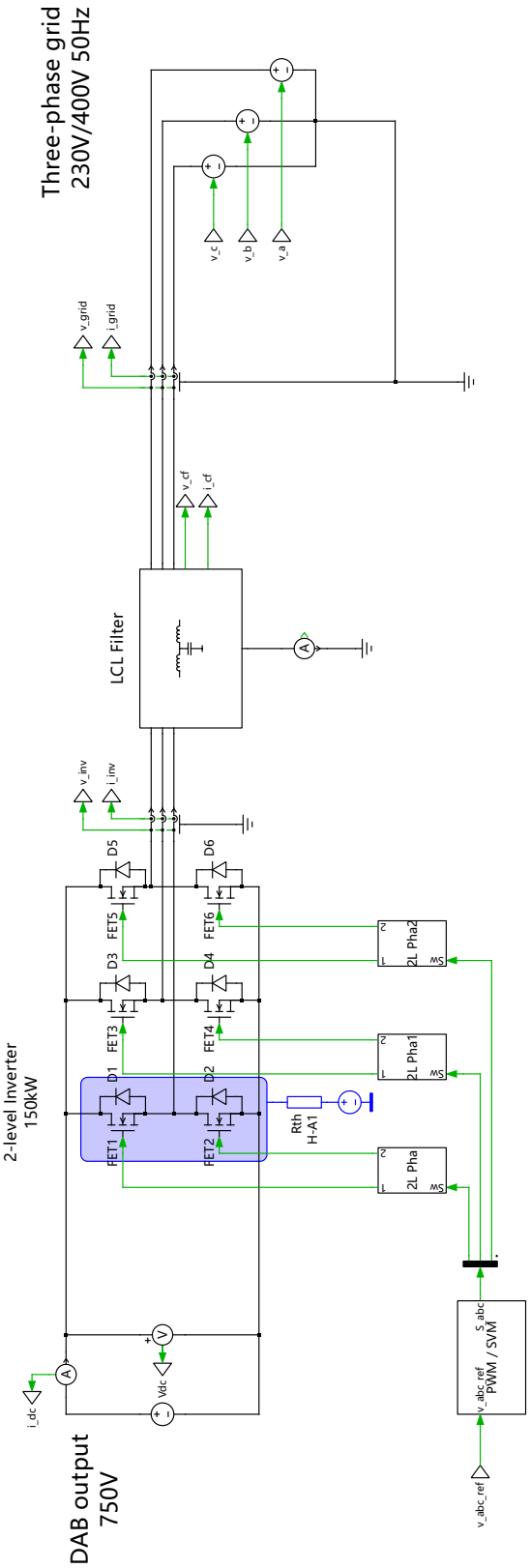
Three-phase grid
230V/400V 50Hz
v_c
v_b
v_a
v_grid
i_grid
v_cf
i_cf
LCL Filter
v_inv
i_inv
D5
D6
FET5
FET6
D3
D4
FET3
FET4
D1
D2
FET1
FET2
2-level Inverter
150kW
Rth
H-A1
2L Pha2
2L Pha1
2L Pha
SW
v_abc_ref
PWM / SVM
S_abc
Vdc
i_dc
DAB output
750V

(a)

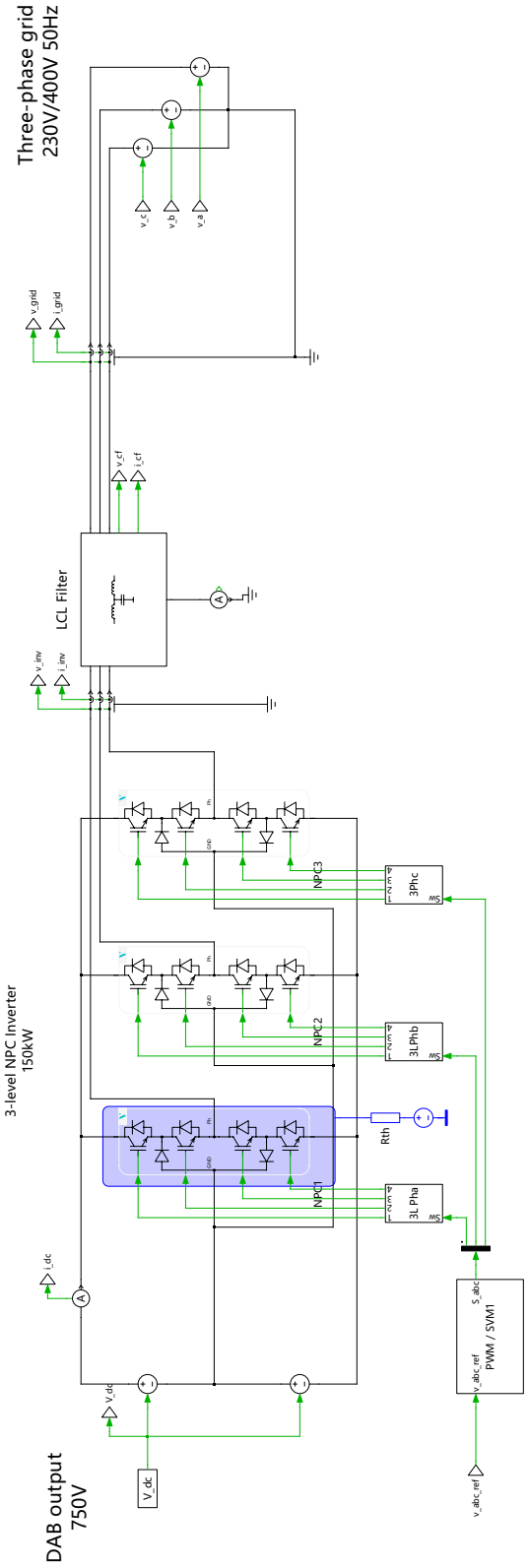

(b)

Figure 3.12: HFT-based System Schematics with Two types of Inverter (a) 2-level inverter, (b) 3-level NPC inverter

4

Results

This chapter presents the simulation and analysis results of the proposed grid-tied power converter systems. Both the LFT-based system and the HFT-based system are evaluated in terms of control performance, voltage regulation, and efficiency under various operating conditions. Detailed comparisons between inverter topologies, transformer types, and isolation strategies are provided to assess the trade-offs in system design, particularly focusing on energy efficiency. All results are obtained using time-domain simulations in PLECS and are supported by practical parameter measurements where applicable.

4.1 Overview of Simulation

Simulations were carried out using MATLAB and PLECS under different power transfer conditions for both systems and the general setup are:

Table 4.1: General Setup of LFT and HFT System

System	Rated Power	DC-link Volatge	Grid Condition	Switching frequency
LFT-based	150 kW	600 V-750 V	400 V RMS, 50 Hz	8 kHz (Inverter)
HFT-based	150 kW	600 V-750 V	400 V RMS, 50 Hz	8 kHz (Inverter), 98 kHz (DAB)

4.2 Control Performance Evaluation

4.2.1 PR Controller Performance (Both Systems)

Figure 4.1 shows the output current waveform of the grid-tied inverter under a 150 kW load and 750 V input using the PR controller. The sinusoidal current closely tracks the reference with negligible steady-state error. The total harmonic distortion (THD) was measured at 6.3% for 2-level inverter and 2.1% for NPC inverter.

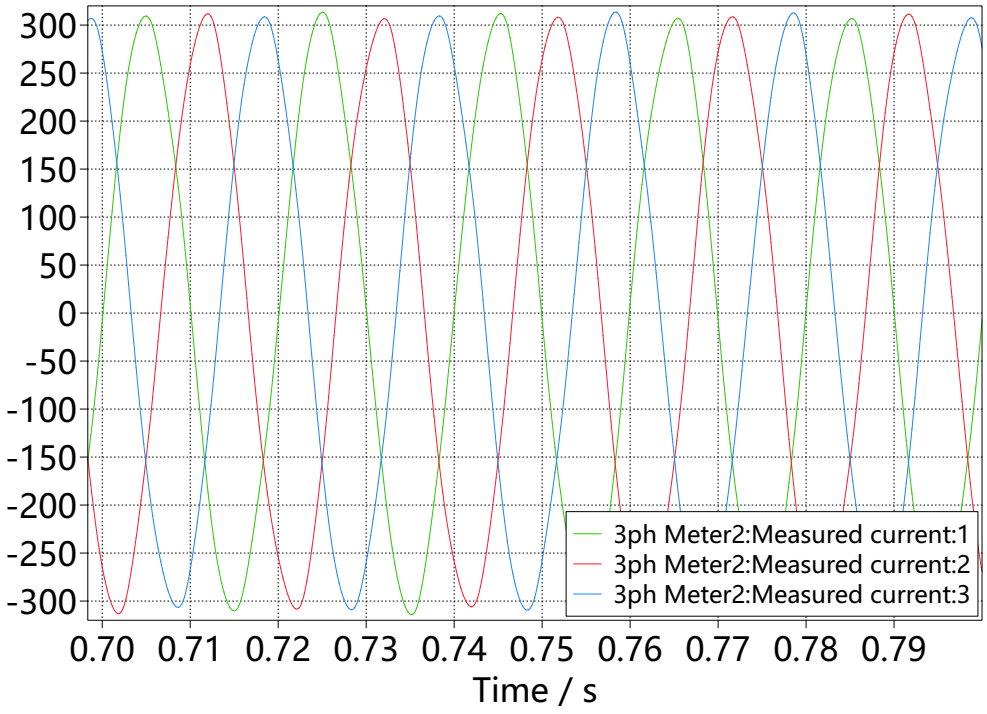

(a)

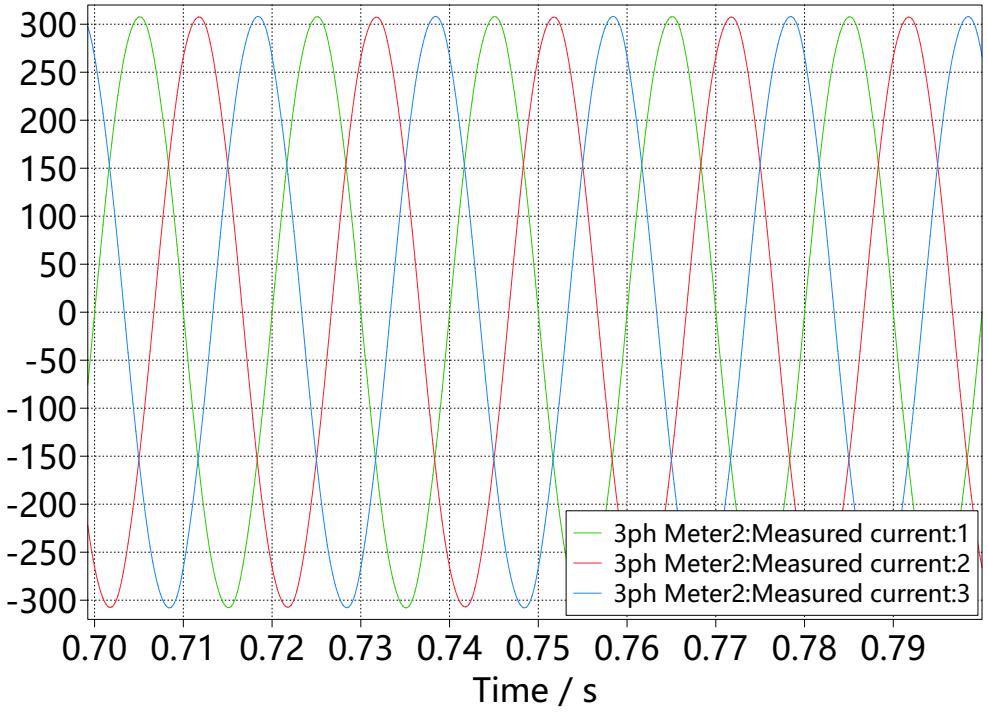

(b)

Figure 4.1: 3-phase Current Waveform
(a). With 2-level inverter
(b). With 3-level NPC inverter

4.2.2 DAB Phase Shift Control (HFT System)

As shown in Figure 4.2, the measured output voltage V_o (green) closely follows the reference voltage (red), with minimal steady-state error. The voltage remains within a tight band of ±1 V (±0.13%) under 600 V input voltage and 30 kW output power, demonstrating the controller's high precision and stability. This confirms the effectiveness of the PI-tuned phase shift control method under nominal loading conditions.

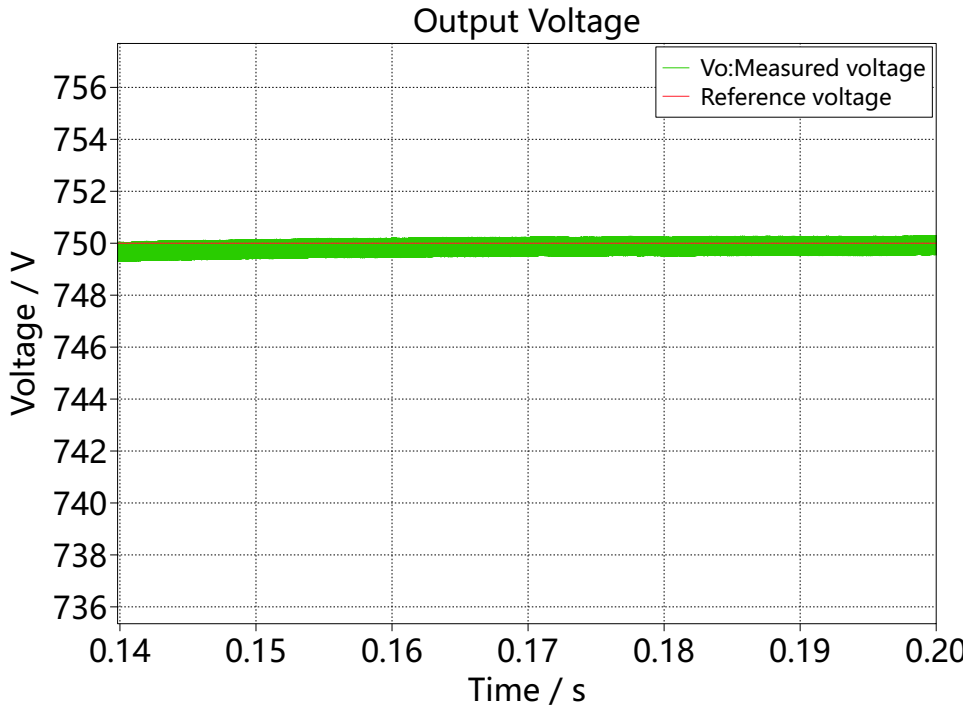

Figure 4.2: Output Voltage of DAB Converter

4.3 Efficiency

4.3.1 LFT System Efficiency

4.3.1.1 Results

Figures 4.3 illustrate the coordinated efficiency maps for each topology: a conventional 2-level inverter (Figure 4.3a) and a 3-level NPC inverter (Figure 4.3b). Both maps demonstrated efficiency as a function of DC input voltage (600–750 V) and output power (10–150 kW).

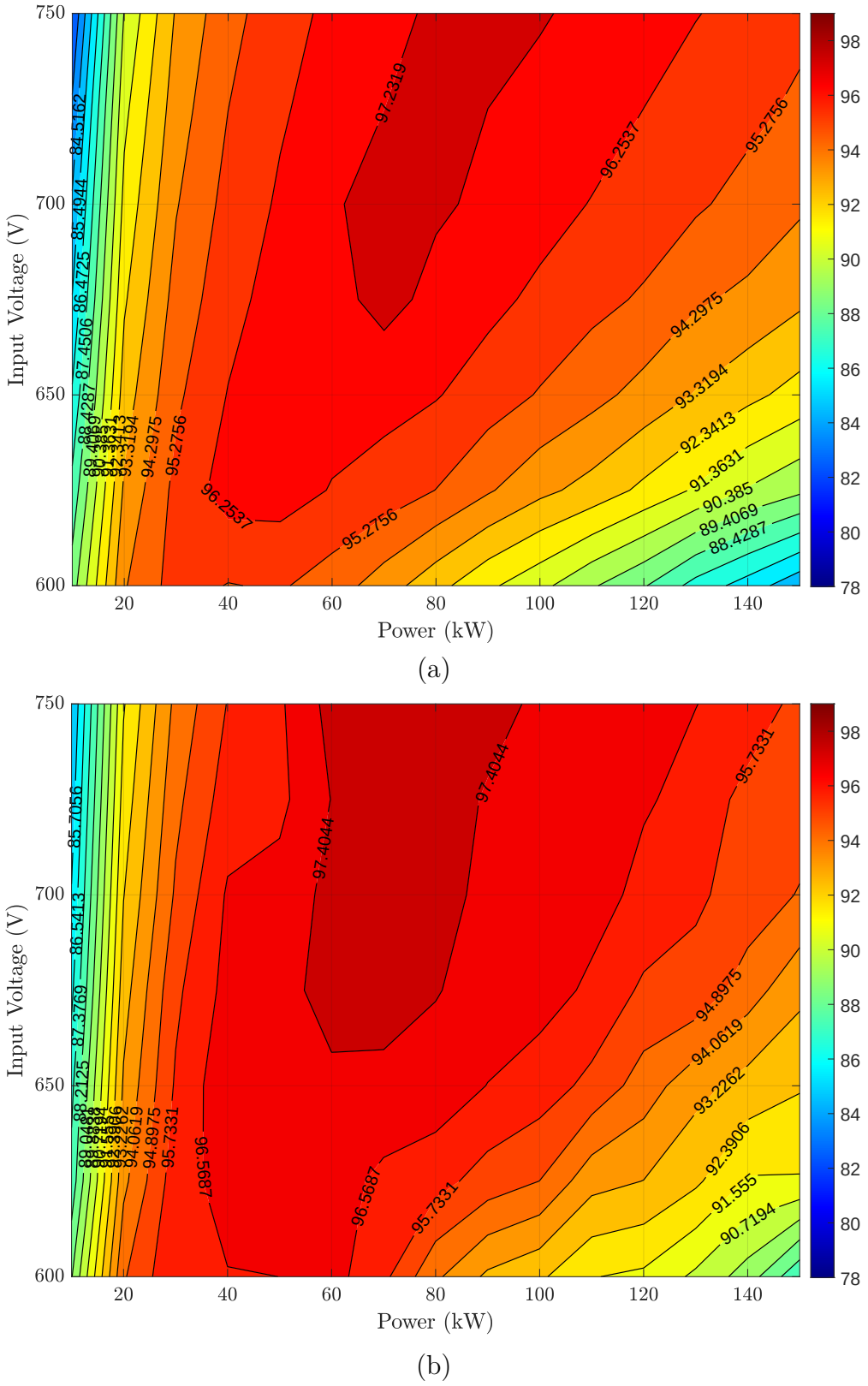

Figure 4.3: Overall Efficiency of LFT System
a. With 2-level inverter
b. With 3-level NPC inverter

4.3.1.2 Discussion

Figure 4.3 compares the overall system efficiency of the LFT-based systems using two different inverter topologies. In the low power and low voltage region, both inverters perform similarly, with overall efficiency below 95%. This is primarily due to transformer core losses, which are relatively constant and dominate at light load. In this region, inverter losses (both conduction and switching) are minimal, and thus the influence of inverter topology is less significant.

As power increases, particularly beyond 50 kW, and as the DC voltage rises above 650 V, a clear performance gap emerges. The 3-level NPC inverter consistently outperforms the 2-level inverter across most of the higher power range. At a representative operating point of 700 V and 100 kW, the 2-level inverter system achieves 96.4% efficiency, while the NPC inverter reaches 97.1%, reflecting a 0.7% improvement which is attributed by two main factors:

- Reduced voltage stress per switch in the NPC inverter, which leads to lower switching and conduction losses.
- Lower harmonic content in the NPC inverter's output voltage, reducing current ripple losses.

Overall, the NPC topology offers improved energy conversion performance for high-power operation, making it more suitable for heavy-duty BESS applications, where maximizing efficiency translates directly to improved thermal management and longer lifetime.

4.3.2 HFT System Efficiency

4.3.2.1 Results

The overall efficiency of the DAB stage was evaluated across a range of input voltages (600–750 V) and input power levels (2–30 kW), as shown in Figure 4.4. The DAB converter achieves peak efficiency above 97% at medium to high input power levels and voltages closer to 750 V.

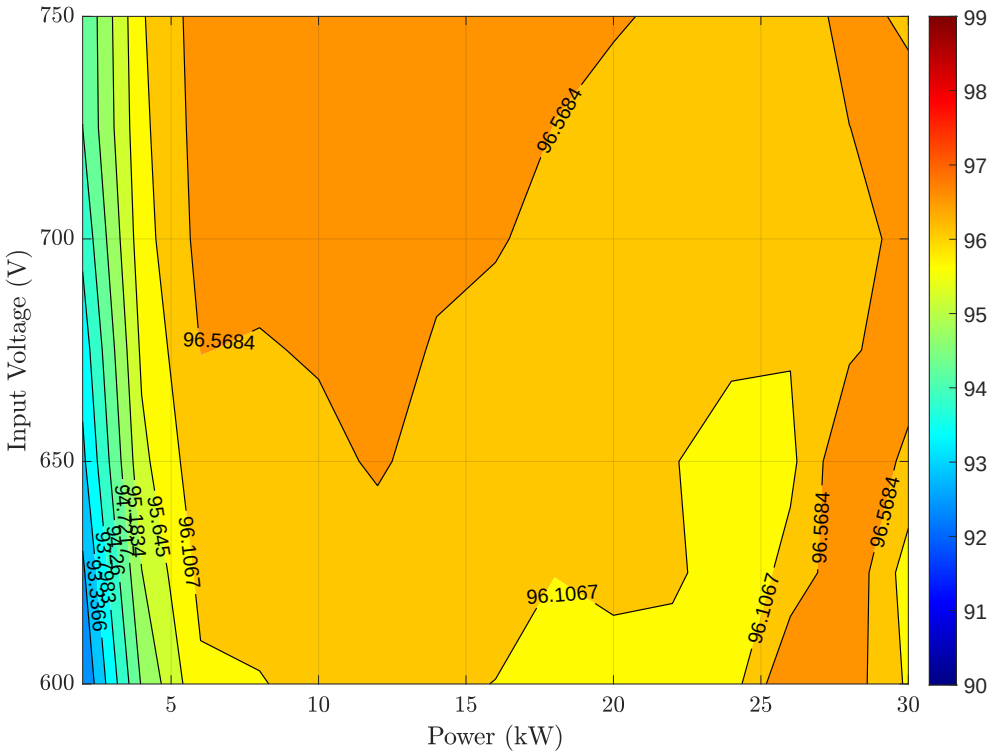

Figure 4.4: Efficiency of DAB Converter

Figures 4.5(a) and (b) compare the efficiency curves of the 2-level VSI and the 3-level NPC inverter used in the HFT system. Both inverters are evaluated over a wide power range (10–150 kW) using the same LCL filter and control methods (PR + SVPWM), supplied by the DAB-regulated 750 V DC link.

1. The 2-level inverter achieves an efficiency of:
   - $\sim$ 91.5% at 20 kW
   - Peaking at 96.7% at 150 kW

2. The 3-level NPC inverter shows a improvement, with:
   - $\sim$ 92.1% at 20 kW
   - Peaking at 98% at 150 kW

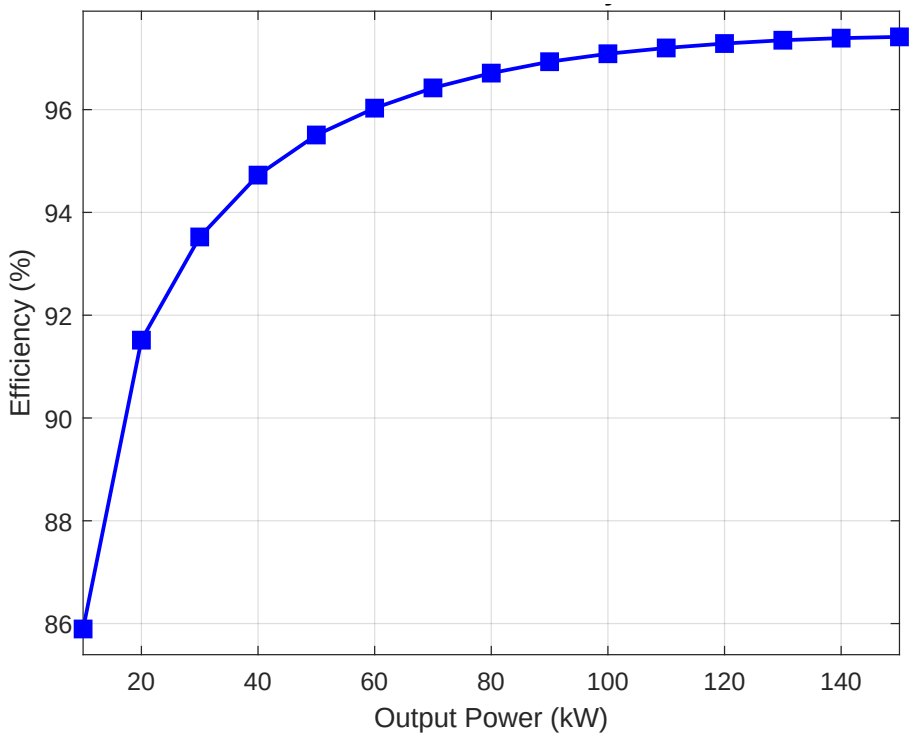

(a)

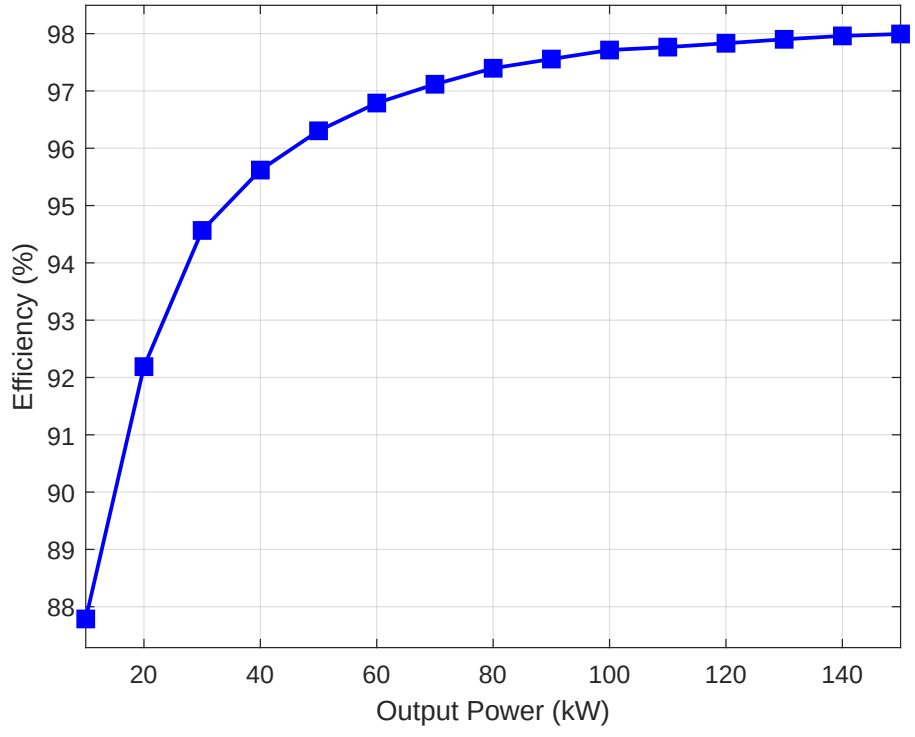

(b)

Figure 4.5: Efficiency Curves
a. With 2-level inverter
b. With 3-level NPC inverter

4.3.2.2 Discussion

The overall Efficiency of DAB converter can be achieved around 96.5%, particularly in the power range of 5–25 kW. However, the DAB efficiency shows a dip at low input voltages and very light load, due to increased core and switching losses dominating total power. This suggests that the DAB is best utilized near its rated load and voltage for maximum efficiency.

Both efficiency curves of the 2-level and 3-level inverter systems demonstrate increasing efficiency with load. The 2-level inverter peaks at 96.7%, while The 3-level NPC inverter achieves a higher peak of 98%. The difference of their efficiency becomes more noticeable at medium to high power, making the NPC inverter more suitable for full-range operation.

When combined, the HFT system maintains consistently high efficiency, particularly when:

- The DAB operates in its optimal power range (10–30 kW per module)
- The inverter operates above 50 kW output where switching losses are less dominant

The modular nature of the DAB provides flexibility and good partial-load performance, but also introduces control and loss variations depending on how modules are activated.

4.3.3 LFT vs. HFT(DAB)

4.3.3.1 Results

To evaluate the impact of the isolation method on system performance, the efficiency of a traditional LFT and a parallelized DAB converter architecture was compared over the full inverter output range of 10–150 kW under 700V DC-link voltage. The results are presented in Figure 4.6(a) for the LFT and Figure 4.6(b) for the DAB configuration.

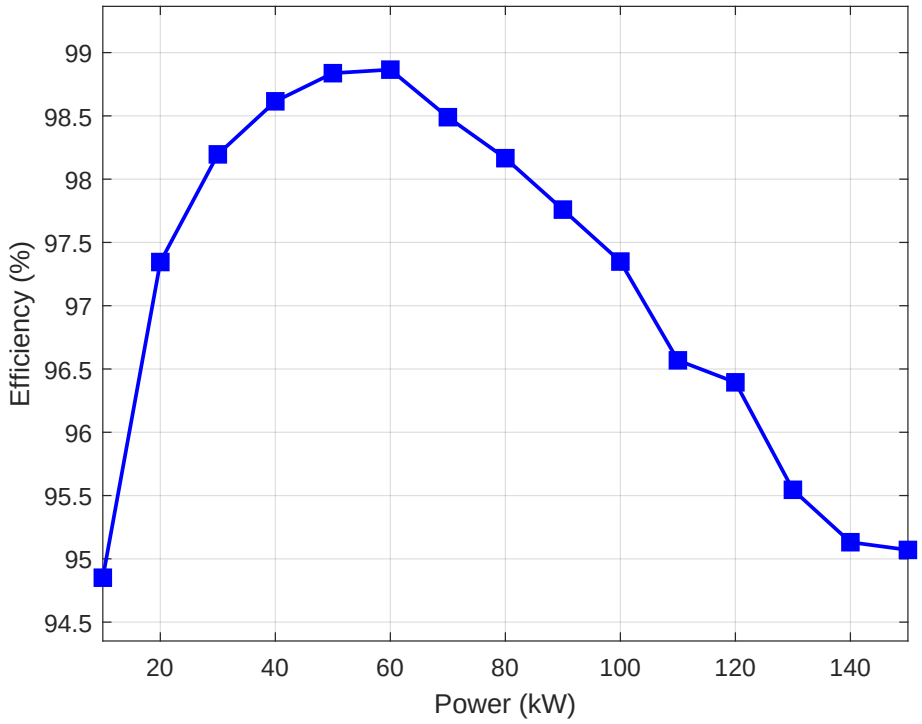

(a)

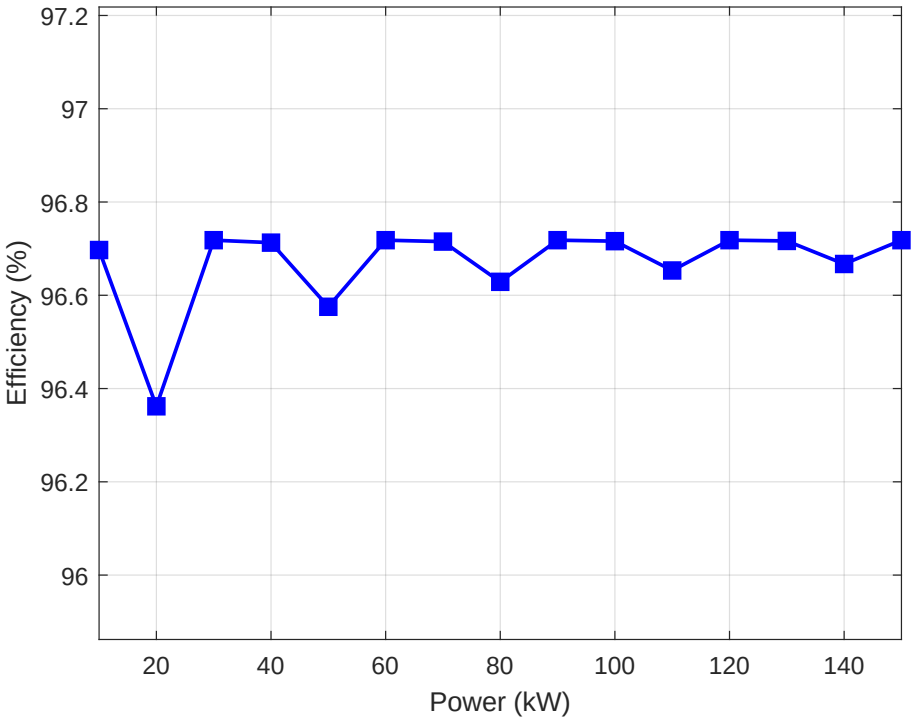

(b)

Figure 4.6: Efficiency Curve of
a. Line Frequency Transformer
b. Parallel DAB Converter

4.3.3.2 Discussion

As shown in Figure 4.6(a), the LFT exhibits relatively low efficiency at low output power levels, starting at 94.7% at 10 kW. This is due to the constant core losses and magnetizing losses, which remain large regardless of load. However, as power increases, the proportion of these fixed losses relative to output power decreases, causing overall efficiency to rise, reaching 98.8% at 60 kW. Beyond the peak efficiency point (60 kW), the copper losses become dominant. These increase with the square of the load current $P_{\text{cu}} \propto I^2R$, the large current flow causes significant losses in the transformer windings at high load. Therefore, the efficiency begins to gradually decline.

To match the 150 kW inverter output capacity using DAB modules limited to 30 kW each, six DAB converters were connected in parallel. In this simulation, DAB converters are activated sequentially, i.e., one converter operates at full load before the next is turned on, rather than evenly distributing the power among all six.

The efficiency of the DAB system is shown in Figure 4.6(b). Each DAB maintains a high and stable efficiency between 96.4% and 96.8% across its operating range. Despite some fluctuation due to the sequential control strategy, the overall system performance remains consistent. Unlike the LFT, the DAB efficiency does not rise significantly with power, as the core and switching losses are already optimized at each module's nominal point.

We can conclude from results that:

- The LFT efficiency peaks at mid-load but drops at high power from increased copper loss.
- The DAB configuration maintains consistently high efficiency and offers modular scalability and better power density.

This comparison highlights a key trade-off between load-dependent performance of LFTs and the modularity and flexibility of DAB-based architectures in grid-connected BESS applications.

5
Conclusion

This thesis presented the design, control, and performance evaluation of grid-tied power electronic converters for BESS, focusing on two isolation approaches: a LFT-based system and a HFT-based system utilizing parallel DAB converters. Both architectures were modeled and simulated using MATLAB and PLECS, with emphasis on transformer modeling, loss analysis, and overall system efficiency.

For the inverter stage, a PR controller combined with space vector PWM was implemented to achieve fast dynamic response and zero steady-state error. In the HFT system, a phase shift controller was designed to regulate power flow through the DAB by adjusting the phase angle between primary and secondary bridges, ensuring soft switching and stable output voltage regulation.

The LFT system exhibited high efficiency at mid-load, benefiting from minimal power-dependent losses in the transformer. However, it showed decreased performance at low and high loads due to core losses and copper losses. In contrast, the HFT-based system achieved consistently high efficiency across a wider load range and offered superior power density and modularity by using multiple DAB converters. Although, the complexity of control and the need for careful loss management in high-frequency designs were noted.

Simulation results demonstrated that both systems are capable of delivering high efficiency and grid compliance, but the HFT-based solution is more suitable for applications requiring compactness and flexible power scaling.

While the results confirm the technical feasibility and benefits of both systems, there remain several important works for future research:

- Experimental validation: Building a hardware prototype, especially of the HFT-based system, would allow for the verification of simulation results under real-world conditions, including thermal behavior, EMI performance, and controller robustness.
- Multiple DAB control method: This thesis implemented sequential control of DAB modules. Future work could explore more advanced power-sharing strategies.
- Fault handling and protection: Developing fault detection and protection mechanisms, particularly for parallel DAB architectures, would improve reliability in pratical applications.

By addressing these research directions, the findings of this thesis can be extended to support the design of next-generation, high-performance BESS in marine, industrial, and renewable energy applications.

Bibliography

[1] Y. Li, Y. Chi, X. Wang, X. Tian and J. Jianqing, "Practices and Challenge on Planning with Large-scale Renewable Energy Grid Integration," 2019 IEEE 3rd Conference on Energy Internet and Energy System Integration (EI2), Changsha, China, 2019, pp. 118-121, doi: 10.1109/EI247390.2019.9062091.

[2] N. W. Miller, R. S. Zrebiec, R. W. Delmerico and G. Hunt, "Battery energy storage systems for electric utility, industrial and commercial applications," Proceedings of 11th Annual Battery Conference on Applications and Advances, Long Beach, CA, USA, 1996, pp. 235-240, doi: 10.1109/BCAA.1996.485001.

[3] A. Oudalov, D. Chartouni, C. Ohler and G. Linhofer, "Value Analysis of Battery Energy Storage Applications in Power Systems," 2006 IEEE PES Power Systems Conference and Exposition, Atlanta, GA, USA, 2006, pp. 2206-2211, doi: 10.1109/PSCE.2006.296284.

[4] Bolun Xu, Alexandre Oudalov, Jan Poland, Andreas Ulbig, Göran Andersson, "BESS Control Strategies for Participating in Grid Frequency Regulation", IFAC Proceedings Volumes, Volume 47, Issue 3, 2014, Pages 4024-4029, doi: 10.3182/20140824-6-ZA-1003.02148.

[5] Chunyang Zhao, Peter Bach Andersen, Chresten Træholt, Seyedmostafa Hashemi, "Grid-connected battery energy storage system: a review on application and integration", Renewable and Sustainable Energy Reviews, Volume 182, 2023, doi: 10.1016/j.rser.2023.113400.

[6] Kisuk Kim, Taeyoung Yoon, Gilsung Byeon, Hosung Jung, Hyoungchul Kim and Gilsoo Jang, "Power demand and power quality analysis of EV charging station using BESS in MicroGrid," 2012 IEEE Vehicle Power and Propulsion Conference, Seoul, Korea (South), 2012, pp. 996-1001, doi: 10.1109/VPPC.2012.6422752.

[7] M. Yilmaz and P. T. Krein, "Review of the Impact of Vehicle-to-Grid Technologies on Distribution Systems and Utility Interfaces," in IEEE Transactions on Power Electronics, vol. 28, no. 12, pp. 5673-5689, Dec. 2013, doi: 10.1109/TPEL.2012.2227500.

[8] F. Sun, S. Li, Y. Liu, C. Xie, Q. Zhao and Y. Shi, "The Power Electronic Transformer based Multi-port DC Charging Station," 2020 12th IEEE PES Asia-Pacific Power and Energy Engineering Conference (APPEEC), Nanjing, China, 2020, pp. 1-5, doi: 10.1109/APPEEC48164.2020.9220544.

[9] W. Choi, W. Lee and B. Sarlioglu, "Effect of grid inductance on grid current quality of parallel grid-connected inverter system with output LCL filter and closed-loop control," 2016 IEEE Applied Power Electronics Conference

and Exposition (APEC), Long Beach, CA, USA, 2016, pp. 2679-2686, doi: 10.1109/APEC.2016.7468242.

[10] Y. Chen, Z. Zhang, Q. Li and P. Zou, "Stability Analysis and Inspection of Grid-connected Inverter in Large-scale New Energy Environment," 2021 6th International Conference on Power and Renewable Energy (ICPRE), Shanghai, China, 2021, pp. 487-492, doi: 10.1109/ICPRE52634.2021.9635371.

[11] L. Wang, Z. Qin, T. Slangen, P. Bauer and T. van Wijk, "Grid Impact of Electric Vehicle Fast Charging Stations: Trends, Standards, Issues and Mitigation Measures - An Overview," in IEEE Open Journal of Power Electronics, vol. 2, pp. 56-74, 2021, doi: 10.1109/OJPEL.2021.3054601.

[12] V. Fernão Pires, Enrique Romero-Cadaval, D. Vinnikov, I. Roasto, J.F. Martins, "Power converter interfaces for electrochemical energy storage systems – A review", Energy Conversion and Management, Volume 86, 2014, Pages 453-475, doi: 10.1016/j.enconman.2014.05.003.

[13] Shariff, Samir Alam, Mohammad Hameed, Salman Khalid, Mohd Ahmad, Aqueel Al-Ammar, Essam Alsaidan, Ibrahim Alrajhi, Hasan, "A State-of-the-Art Review on the Impact of Fast EV Charging on the Utility Sector", Energy Storage, Volume 4, 2021, doi: 10.1002/est2.300.

[14] L. Paul, A. M. Mathew, A. Meethian and S. Sharief, "Power Electronic Traction Transformer with Minimum Losses," 2023 International Conference on Innovations in Engineering and Technology (ICIET), Muvattupuzha, India, 2023, pp. 1-7, doi: 10.1109/ICIET57285.2023.10220578.

[15] M. M. Haque, P. Wolfs, S. Alahakoon, B. C. P. Sturmberg, M. Nadarajah and F. Zare, "DAB Converter With Q Capability for BESS/EV Applications to Allow V2H/V2G Services," in IEEE Transactions on Industry Applications, vol. 58, no. 1, pp. 468-480, Jan.-Feb. 2022, doi: 10.1109/TIA.2021.3123139.

[16] S. Sitompul and G. Fujita, "Implementation of BESS Load Frequency Control in Islanded Microgrid System by Considering SOC," 2020 IEEE PES Innovative Smart Grid Technologies Europe (ISGT-Europe), The Hague, Netherlands, 2020, pp. 980-984, doi: 10.1109/ISGT-Europe47291.2020.9248945.

[17] J. A. P. Lopes, C. L. Moreira and A. G. Madureira, "Defining control strategies for MicroGrids islanded operation," in IEEE Transactions on Power Systems, vol. 21, no. 2, pp. 916-924, May 2006, doi: 10.1109/TPWRS.2006.873018.

[18] R. Teodorescu, F. Blaabjerg, M. Liserre, and P.C. Loh, "Proportional-resonant controllers and filters for grid-connected voltage-source converters," in IEE Proceedings -Electric Power Applications, Vol. 153, Issue 5, 2006, doi: 10.1049/ip-epa:20060008.

[19] M.P. Kazmierkowski, R. Krishnan, F. Blaabjerg, "Control in Power Electronics Selected Problems", (Academic Press, 2002)

[20] S. Shao et al., "Modeling and Advanced Control of Dual-Active-Bridge DC–DC Converters: A Review," in IEEE Transactions on Power Electronics, vol. 37, no. 2, pp. 1524-1547, Feb. 2022, doi: 10.1109/TPEL.2021.3108157.

[21] B. Zhao, Q. Song, W. Liu and Y. Sun, "Overview of Dual-Active-Bridge Isolated Bidirectional DC–DC Converter for High-Frequency-Link Power-Conversion System," in IEEE Transactions on Power Electronics, vol. 29, no. 8, pp. 4091-4106, Aug. 2014, doi: 10.1109/TPEL.2013.2289913.

[22] Y. H. Xie, J. Sun and S. F. James, "Power flow characterization of a bidirectional galvanically isolated high-power DC/DC converter over a wide operating range", IEEE Trans. Power Electron., vol. 25, no. 1, pp. 54-65, Jan. 2010.

[23] B. Zhao, Q. Yu and W. Sun, "Extended-Phase-Shift Control of Isolated Bidirectional DC–DC Converter for Power Distribution in Microgrid," in IEEE Transactions on Power Electronics, vol. 27, no. 11, pp. 4667-4680, Nov. 2012, doi: 10.1109/TPEL.2011.2180928.

[24] Guohong Zeng, T. W. Rasmussen, Lin Ma and R. Teodorescu, "Design and control of LCL-filter with active damping for Active Power Filter," 2010 IEEE International Symposium on Industrial Electronics, Bari, Italy, 2010, pp. 2557-2562, doi: 10.1109/ISIE.2010.5637575.

[25] Y.-J. Kim, H. Kim, "Optimal design of LCL filter in grid-connected inverters," IET Power Electronics, vol. 12, no. 7, pp. 1774-1782, 2016, doi: 10.1049/iet-pel.2018.5518.

[26] F. Li, X. Zhang, H. Zhu, H. Li and C. Yu, "An LCL-LC Filter for Grid-Connected Converter: Topology, Parameter, and Analysis," in IEEE Transactions on Power Electronics, vol. 30, no. 9, pp. 5067-5077, Sept. 2015, doi: 10.1109/TPEL.2014.2367135.

[27] M. Liserre, F. Blaabjerg and S. Hansen, "Design and control of an LCL-filter-based three-phase active rectifier," in IEEE Transactions on Industry Applications, vol. 41, no. 5, pp. 1281-1291, Sept.-Oct. 2005, doi: 10.1109/TIA.2005.853373.

[28] T. Basarik, M. Lacko, M. Pástor, D. Gordan and T. Kmecik, "Iterative Method for Estimating the Parameters of a Linear Transformer Model," 2024 ELEKTRO (ELEKTRO), Zakopane, Poland, 2024, pp. 1-5, doi: 10.1109/ELEKTRO60337.2024.10557015.

[29] V. Del Toro, Principles of Electrical Engineering, 2nd ed. Englewood Cliffs, NJ: Prentice-Hall, 1972.

[30] S. V. Araujo, P. Zacharias and R. Mallwitz, "Highly Efficient Single-Phase Transformerless Inverters for Grid-Connected Photovoltaic Systems," in IEEE Transactions on Industrial Electronics, vol. 57, no. 9, pp. 3118-3128, Sept. 2010, doi: 10.1109/TIE.2009.2037654.

[31] W. Choi, D. Han, C. T. Morris and B. Sarlioglu, "Achieving high efficiency using SiC MOSFETs and reduced output filter for grid-connected V2G inverter," IECON 2015 - 41st Annual Conference of the IEEE Industrial Electronics Society, Yokohama, Japan, 2015, pp. 003052-003057, doi: 10.1109/IECON.2015.7392568.

[32] Kuder, Manuel, Anton Kersten, Jose-Luis Marques-Lopez, Julian Estaller, Johannes Buberger, Florian Schwitzgebel, Torbjörn Thiringer, Anton Lesnicar, Rainer Marquardt, Thomas Weyh, and et al. 2022. "Capacitor Voltage Balancing of a Grid-Tied, Cascaded Multilevel Converter with Binary Asymmetric Voltage Levels Using an Optimal One-Step-Ahead Switching-State Combination Approach" Energies 15, no. 2: 575. https://doi.org/10.3390/en15020575

[33] K. George, "Design and Control of a Bidirectional Dual Active Bridge DC-DC Converter to Interface Solar, Battery Storage, and Grid-Tied

Inverters. Electrical Engineering Undergraduate Honors Theses", 2015, https://scholarworks.uark.edu/eleguht/45

DEPARTMENT OF SOME SUBJECT OR TECHNOLOGY
CHALMERS UNIVERSITY OF TECHNOLOGY
Gothenburg, Sweden
www.chalmers.se

CHALMERS
UNIVERSITY OF TECHNOLOGY